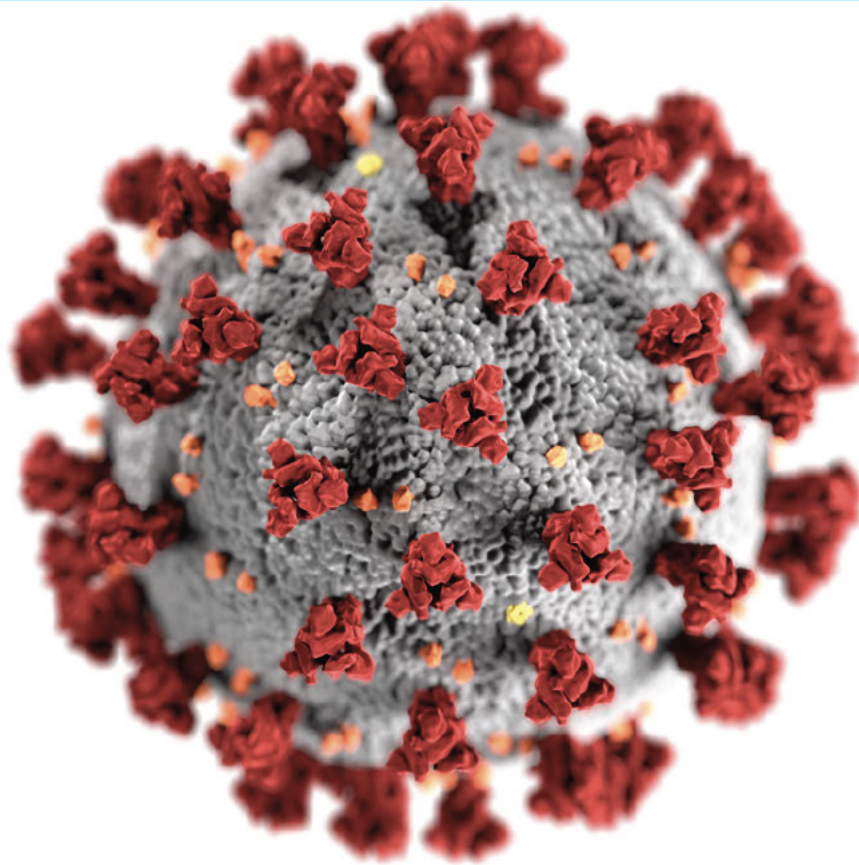


Non-Invasive Screening for Elevated Skin Temperature and Respiratory Rate related to COVID-19 using Thermal Imaging

A.J. Thomas

Master Thesis Project
March 30, 2021



Non-Invasive Screening for Elevated Skin Temperature and Respiratory Rate related to COVID-19 using Thermal Imaging

Name	A.J. Thomas		
Student Number	4916123		
Programme	M.Sc Biomedical Engineering		
Thesis Supervisors	Dr. Hen-Wei Huang, MIT	Prof. Giovanni Traverso, MIT	
	Ir. Kianoush Rassels, TU Delft	Prof. Paddy French, TU Delft	



Contents

- Acknowledgements 1
- Abstract 2
- 1 Introduction 3
 - 1.1 General Introduction 3
 - 1.2 Problem Overview - Clinical Need for Remote Screening 4
 - 1.3 Thesis Objectives 5
 - 1.4 Structure of the Thesis 5
- 2 Background Information and System 6
 - 2.1 Skin Temperature - Theory, Location Choice 6
 - 2.1.1 Human Body Thermo-regulation 6
 - 2.1.2 Heat Transfer from Skin 8
 - 2.1.3 Evaluation of Elevated Skin Temperature Region of Interest 8
 - 2.1.4 Measurement Location for Elevated Skin Temperature screening 10
 - 2.2 Respiration - Theory, Location Choice 10
 - 2.2.1 Heat Transfer from Nose 11
 - 2.2.2 Evaluation of Respiration Region of Interest 11
 - 2.2.3 Measurement Location for Abnormal Respiration Screening. 11
 - 2.3 Theory 12
 - 2.3.1 IR Radiation 12
 - 2.3.2 Heat Transfer variation with Ambient Temperature and Distance 14
 - 2.3.3 Camera Pixel Spatial Coverage 14
 - 2.3.4 Distance Estimation using Image Information 15
 - 2.3.5 Signal Extraction and Filtering for Abnormal Respiration Screening 16
 - 2.4 System Outline 17
 - 2.4.1 Hardware and Communication Interface of the System 18

2.4.2	Image Processing of Thermal Camera Frames	18
2.5	Choice of Hardware and Software for the Prototype	24
2.5.1	IR Camera Technology and Selection	24
2.5.2	GPU for Implementation of Face Detection	26
2.5.3	Environmental Sensor, Interfacing and Supporting Equipment	27
2.6	Mask Detection	31
2.7	Elevated Skin Temperature and Abnormal Respiration Screening	32
2.8	Chapter Conclusions	34
3	Research, Methods and Validation	36
3.1	Camera Specific Procedures.	36
3.1.1	Camera Accuracy	36
3.1.2	Camera Spatial Coverage.	37
3.2	Evaluation of Bounding Box Vectors using Head Pose Experiments	37
3.3	Distance and Temperature Estimation	39
3.3.1	Modelling of Distance and Experiments	39
3.3.2	Measurement of Distance and Height vector.	40
3.3.3	Skin Temperature Measurement at varying Ambient Temperature and Distance.	41
3.3.4	Slope Extracted from Measured Skin Temperature versus Ambient Temperature.	42
3.3.5	Adaptive Temperature Compensation Model using Slope Calculation	43
3.4	Respiration Visualisation and Respiratory Rate Calculation	44
3.5	Validation.	46
3.5.1	Region of Interest for Elevated Skin Temperature Screening	46
3.5.2	Subject Distance from the Camera	48
3.5.3	Temperature Compensation Model	49
3.5.4	Mask Detection	49
3.5.5	Respiratory Rate	50
3.6	System Benchmark	51
3.7	Chapter Conclusions	51
4	Conclusions and Future work	52
4.1	Conclusions.	52
4.2	Future work.	53

A Appendix	55
A.1 General Requirements	55
A.2 Project Requirement Analysis	55
A.2.1 Functional Requirements	55
A.2.2 Non-Functional Requirements.	57
A.3 Horizontal and Vertical Displacement from Optic Center	57
A.4 System Run Time	58
A.5 Ethical Considerations	58
List of Figures	59
List of Tables	63
List of Abbreviations	64
List of Symbols	66
Bibliography	69

Acknowledgements

This graduation project could not have been possible without the support of many people. My thesis supervisor, Dr Hen-Wei Huang, has helped me throughout the project. He has made sure to give access to multiple resources during the lockdown. His brilliance in the field never surprises me. I would also like to thank Prof. Giovanni Traverso for his guidance and support during the project. I am thankful to Prof. Giovanni Traverso and Prof. Robert Langer for giving me this opportunity to work at MIT. I would also like to thank Claas, Can-Chen and my other colleagues for their support and help during the project.

I would also like to extend thanks to Ir. Kianoush Rassels, my advisor at TU Delft, whose constant feedback and support has helped during the course of my thesis project. He has thought me to think critically and to structure my thesis effectively. I would also like to thank Prof. Paddy French, who has been advising throughout the way and helped me shape the thesis report.

I would also like to extend thanks to my family and friends for their constant support throughout the study programme.

Abstract

Non-contact infrared thermal imaging provides a non-invasive, safe and accurate means for screening subjects. COVID-19 (a disease caused by the Severe Acute Respiratory Syndrome Corona Virus 2 (SARS-CoV-2)) has changed how health care workers (HCW) interact with patients. Despite the usage of personal protective equipment (PPE), social distancing protocols and unique facilities to screen individuals, the rate of increase of infection among HCW is high. This has enormous consequences as HCW cannot provide direct patient care, thereby decreasing the workforce's availability during the pandemic. This has fuelled the urgent need for a non-invasive IR system to screen for potential cases of infections. Existing remote screening systems are susceptible to shortcomings caused by location and technique used for measurement, a distance-ambient temperature associated inaccuracies and inefficient integration of hardware and software modules, invalidating their utility in the current situation. During this project, a non-invasive screening prototype was developed that mitigates these shortcomings by using an adaptive measurement method with automatic environmental compensation for screening elevated skin temperature and respiratory rate. The prototype is tested and validated in a temperature-controlled environment.

1

Introduction

1.1. General Introduction

The increase in infection rate among health care workers (HCW) at hospitals can be reduced by the use of remote screening techniques [1] [2]. Effective implementation of a remote screening prototype involves combining different techniques to screen for potential indicators of infection.

Vital Signs as Infection Indicators

Physiological activities occurring within the human body can be understood through the screening and measurement of vital signs [3]. Vital signs include heart rate, blood oxygen saturation, respiratory rate, blood pressure and body temperature. Each of these vital signs corresponds to the functioning of a system of essential organs in the body. The coronavirus disease 2019 (COVID-19) disease most commonly causes an elevated body temperature (fever) and abnormal breathing amongst infected individuals, and screening these symptoms provides valuable initial information regarding potential infection [4].

Types of Screening Techniques

Vital signs screening methodologies are broadly divided into contact-based and non-intrusive systems. Conventional methods to measure vital signs have mostly been contact-based. Contact-based sensors, electrode-based measurement systems, pulse oximeters and implantable sensors are some examples of such technolo-

gies currently having widespread use across the global healthcare sector [5]. These systems face a booming commercial demand, making companies like Fitbit, Apple and Garmin develop products integrated with sensing technologies [6]. Inherent problems faced by these contact-based screening systems include slow-moving advancement due to numerous hurdles like elaborate legal compliance and multi-level trials (for implantable technologies), battery requirements, the accuracy of the data detected and patient subjectivity. Compared to contact-based screening systems, remote non-intrusive screening technologies come with advantages of extreme ease in implementation and large-scale utility. They maintain an aseptic status through the screening process and can be used in places with high contamination risk such as hospital wards, where distancing is necessary and contamination during measurement of vitals poses a risk[1]. They are also relatively easy to deploy across different clinical and non-clinical environments [7].

Automated System for Non-Invasive Screening

Currently, remote screening methodologies need to overcome certain limitations including inefficient multi-subject screening, expensive hardware and factors hindering accuracy in order to be an effective vital sign screening system that can aid in the determination of COVID-19 infection. Hospitals currently employ workers to screen potentially infected patients with close-proximity technology, which significantly compromises their safety, leading to a spike in infections amongst hospital workers. Hence, there is an urgent demand to develop a robust remote high throughput, multi-symptom screening system. The system should be able to screen subjects at different distances and ambient temperatures automatically.

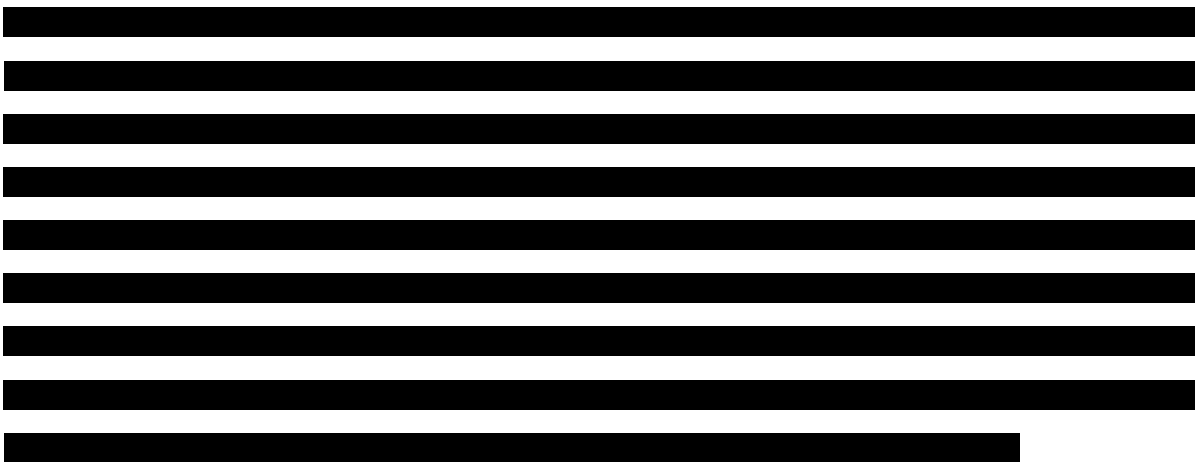
1.2. Problem Overview - Clinical Need for Remote Screening

Hospitals have an urgent need for non-invasive vital signs monitoring as there has been a spike in infections amongst hospital workers, causing widespread concern. Remote screening systems would significantly reduce the risk that most workers currently face while using close-proximity screening, which exposes them significantly to the infection [8]. Studies have shown that infection rates among clinical workers have spiralled, which impedes their capacity to execute tasks [1]. The increase in infection rate is attributed partly to close range screening technology during patient influx in clinics. The goal is to reduce exposure to the disease by installing a remote screening setup. Current elevated skin temperature (EST) screening solutions exhibit problems with measurement accuracy. They utilize fixed distance measurement techniques to measure skin temperature. Screening requires the removal of facial articles like glasses which does not fall within effective health standards. Currently, subjects require to wear masks which pose additional challenges for facial detection and respiratory rate measurement.

1.3. Thesis Objectives

It is necessary to evaluate the exact symptoms that need to be screened to screen subjects in clinics for vital signs. An integrated system implementation for the execution of the technology is essential for implementation. This requires an extensive analysis of hardware and software requirements followed by integration of the different modules. The project is focused on the development of a multi-symptom screening setup which would utilize IR camera technology for the screening of elevated skin temperature and abnormal respiratory rate.

1.4. Structure of the Thesis



2

Background Information and System

Infections in the body can be detected by screening vital signs like body temperature and breathing patterns. The scope of this project requires utilising facial temperature measurement from subjects to evaluate the different vital signs. It is necessary to identify an optimum region of interest (ROI) from the face, which can measure absolute temperature for elevated skin temperature screening and temperature changes in the area around the mouth and nostrils to screen for abnormal breathing among subjects. The screening system implementation requires effectively choosing hardware and software, understanding the working of IR radiation, developing a compensation model for better accuracy, and a technique for abnormal respiration screening. The system outline consists of an overview of the five major blocks (hardware, communication, image processing, screening and user display) that are used for implementing the prototype.

2.1. Skin Temperature - Theory, Location Choice

The skin temperature is dependent on the body's heat control process and varies depending on location in the body. The skin temperature is correlated to the body temperature depending on its location.

2.1.1. Human Body Thermo-regulation

Human body temperature is controlled internally primarily by the endocrine system and hypothalamus in the brain [9]. In addition to this, there are processes like convection, conduction, evaporation and radiation that causes changes in temperature seen in Fig 2.1.

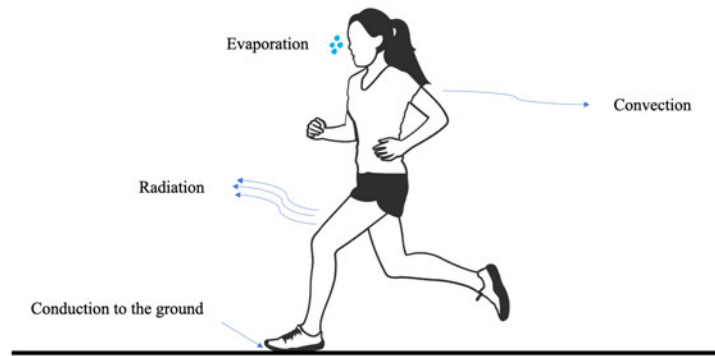


Figure 2.1: An illustration of the various processes (convection, evaporation, radiation and conduction) by which heat is lost to the surrounding from the skin.

The majority of the body's heat loss is due to radiation, which is a loss in the form of infrared (IR) radiation [10]. Heat transfer involves the exchange of thermal energy between different medium. There are generally two different types of temperature that are used while referring to the human body temperature. One is the core body temperature and the other being the skin surface temperature. The core body temperature remains relatively constant and does not vary a lot. The skin surface temperature varies depending on the respective location and environmental conditions. The core body temperature is maintained in the central part of the body where the major organs are located. The core body temperature is around 36°C to 38°C for healthy individuals. There is a temperature difference between the body and the environment, which results in heat being dissipated into the environment [11]. The skin is broadly divided into three layers: epidermis, dermis and fat layer [12]. The corresponding anatomic diagram of the skin is shown in figure 2.2.

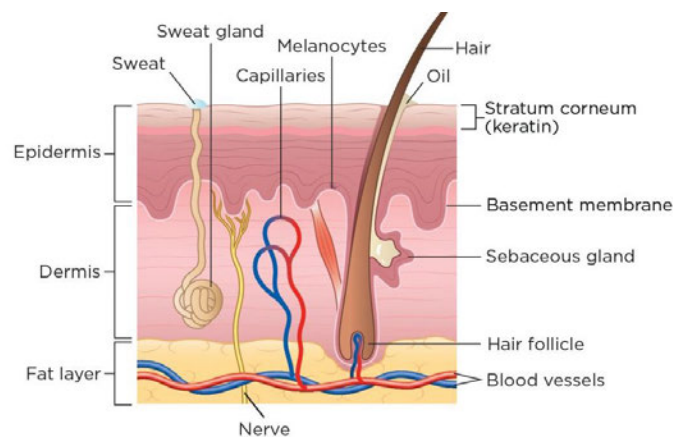


Figure 2.2: The anatomical illustration of the skin (taken from [13]).

The blood from the core of the body travels through the blood vessels around the body. The body's heat balance is maintained depending on the amount of blood flow to the skin's arteries. Using this heat is successfully lost to the environment. The skin surface temperature is correlated with the core body temperature [14]. In the envisioned application, the goal is to estimate the skin surface temperature.

2.1.2. Heat Transfer from Skin

Loss of heat by radiation from the skin is mainly in the form of IR [15]. The net rate of heat transfer by radiation is related to both the object's temperature and its surrounding temperature. The net rate of heat transfer by radiation (n_{rate}) at a particular ambient temperature (T_{amb}) for a surface area (A) can be explained by the equation 2.1 [16].

$$n_{rate} = \epsilon \cdot A \cdot \sigma \cdot (T_{skin}^4 - T_{amb}^4) \quad (2.1)$$

here T_{skin} is the skin surface temperature and ϵ is the emissivity of the surface. Human skin practically behaves like a blackbody ($\epsilon = 1$ in the LWIR region) and this is used consistently with the experiments in the project [17][18][19].

2.1.3. Evaluation of Elevated Skin Temperature Region of Interest

The ROI for measuring temperature is of prime importance for IR thermography, and different studies have evaluated the accuracy and viability of temperature measured from different regions of the face [20]. Since each ROI has advantages and disadvantages, a thorough assessment is necessary before proceeding onto a permanent ROI choice. An ROI at an horizontal angle of less than 60° is most accurate, and the maximum temperature value is the most effective method of measuring ROI temperature [21].

The ear canal, inner canthus, inner mouth and specific side face region close to the temporal artery have the highest correlation with core body temperature [22]. The ear's geometric construction (cylindrical) enables it to serve as a radiation trap, making it an ideal temperature measurement zone. Heat radiation from the tympanic membrane is effectively emitted through the ear [23]. The inner canthus lies directly over important arteries that provide higher blood flow and heat transfer, and skin in this region is less exposed to environmental factors. Inner mouth temperature preserves heat and is directly representative of the core body temperature. The facial region on the side of the face has similar characteristics to the inner canthus regarding skin and artery presence. Temperatures from different ROI is shown in Fig 2.3.

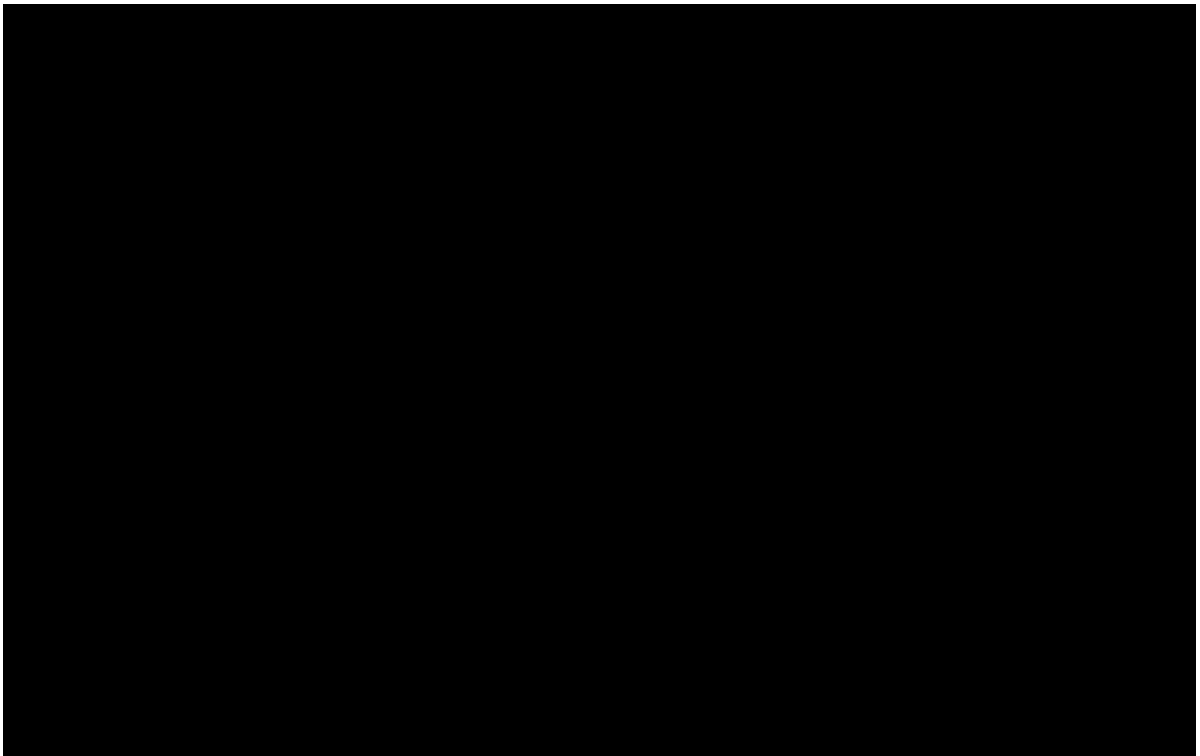


Figure 2.3: Temperature measurements of different ROIs of the face of 10 subjects (data taken from [24]). The ear canal and inner canthus are seen to be the most accurate areas for detection.

Oral temperature is considered the closest to the core body temperature and used as a reference while comparing other regions. Ear canal temperature and inner canthus temperature of the eye are highly correlated to core body temperature. The temperature at the nostrils are highly variable due to respiration and cannot be characterised for screening. Accessibility, in terms of camera viewing angle, to some of these ROIs is extremely low, making them unsuitable for measurement. Additionally, most established facial detection technologies do not identify the ears of subjects or side-face profile, making automatic tracking of such regions unfeasible.

Regions described above, except for the canthi, encounter camera coverage issues due to their location, making them unfeasible for screening. Commonly worn articles like eyeglasses, sunglasses, headphones and face masks make some regions less suitable for screening. The forehead is a widely used ROI for detection as it has the best camera coverage in terms of face angle of viewing and does not suffer from article obstruction but has a low correlation with body temperature [25]. Removal of facial articles while screening hinders infection control protocols and causes widespread implementation problems in the current scenario. For front face features, automatic detection of forehead temperatures offers the best balance between accuracy and accessibility. The forehead is chosen as the best region for temperature measurement from table 2.1.

Part	Position	Impediments	Correlation	Accessibility	Environmental Interference
Ear	Side Face	Ear-accessories	Very High	Low	Low
Inner Canthus	Front Face	Glasses	High	Medium	Low
Forehead	Front Face	None	Medium	High	High
Temple	Side Face	Glasses	High	Low	High
Nose	Front Face	Mask	Low	Low	High
Mouth	Front Face	Mask	Low	Low	Low
Eye	Front Face	Glasses	Medium	Medium	High

Table 2.1: ROI review of the various parts on the face with a list of impediments to the camera view, body temperature correlation, environmental interference and accessibility (in terms of camera view)

2.1.4. Measurement Location for Elevated Skin Temperature screening

The superficial temporary artery region was chosen as the intended location of temperature measurement on the forehead as it has the closest correlation with core body temperature [26]. This correlation makes it the highest temperature region on the face. The superficial temporal artery is also free of thermoregulatory stimuli that cause blood vessel changes [27]. Most of the prominent superficial artery area is found to be within the top 50% of the forehead [28]. Figure 2.4 illustrates the anatomy of the face with the superficial temporal artery.

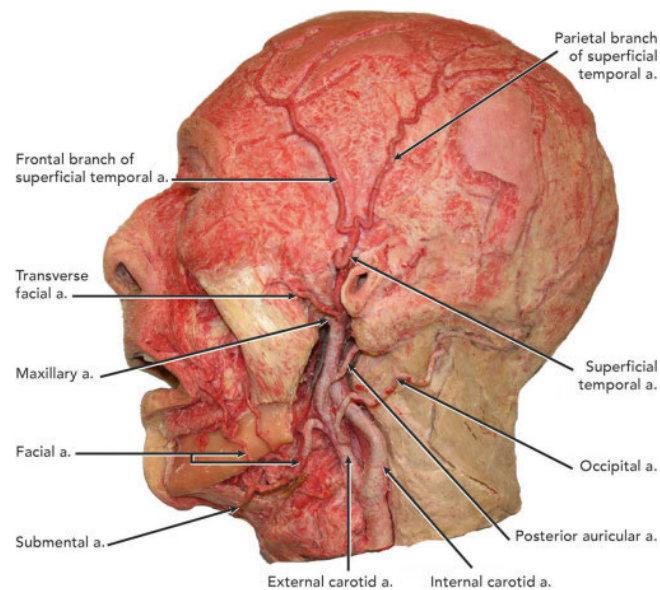


Figure 2.4: The superficial temporal artery location is shown in the photo [29]. The frontal branch of the superficial temporal artery's unique presence across the face ensures its visibility at different angles.

2.2. Respiration - Theory, Location Choice

The following section illustrates the theory for respiration and explains the respiration theory and heat transfer mechanism.

2.2.1. Heat Transfer from Nose

Heat transfer from the nose occurs due to different heat flow components [30]. The convective heat transfer from the nose occurs as a result of airflow over the inner nasal cavity (explained in equation 2.2 [31]).

$$Q_{conv} = k.A_{nasal}.(T_{amb} - T_{nasal}) \quad (2.2)$$

here k is the heat transfer coefficient, A_{nasal} is the internal surface area of the nasal area being transferred, Q_{conv} is the net heat transfer inside the nose as a result of air movement, T_{env} is the environmental temperature, T_{nasal} is the nasal temperature. The observed heat transfer at the nose is the result of the radiated heat at the nostrils (shown in equation 2.3 [30]).

$$Q_{rad} = \epsilon.\sigma.A_c.(T_{nose}^4 - T_c^4) \quad (2.3)$$

here T_{nose} is the nose temperature, T_c is the surrounding temperature. The change in heat energy in the area leads to air temperature change, which is indicative of the respiratory cycle [30].

2.2.2. Evaluation of Respiration Region of Interest

Breathing measurement from an IR camera is done by utilising temperature values from the nasal region. Current health laws mandate the compulsory wearing of masks in public facilities. Measurement of temperature values (for breathing rate) can still be carried out even though the ROI (nose) is covered. [REDACTED]

2.2.3. Measurement Location for Abnormal Respiration Screening

The landmark features from the retina face framework (seen in section 2.15) can be directly used to find the location [32]. There are two feasible approaches: bounding box based and landmark based. The landmarks enable easier tracking of the respiration ROI. The ROI is manually annotated around the respiration zones (nose and mouth). The temperature readings from this region are used for respiratory rate abnormality detection. An example of the region is shown in figure 2.5 below.

2.3. Theory

2.3.1. IR Radiation

Electromagnetic radiation consists of alternating electric and magnetic fields that travel at the speed of light [33]. Sinusoidal EM waves are functions of time and position and with a definite wavelength and frequency [34]. These waves comprise the EM spectrum, such as visible light, IR, X-rays and gamma rays. The energy of the photon (E) increases with an increase in the frequency of radiation shown in equation 2.4 [35].

$$E = h \cdot f = \frac{h \cdot c}{\lambda} \quad (2.4)$$

here, h is planck's constant (6.623×10^{-34} J \cdot s), f is the frequency of the wave, c is the speed of light (3×10^8 m/s) and λ is the wavelength. IR radiation ranges from 0.75 μ m to 300 μ m in the EM spectrum (seen in Fig 2.6).

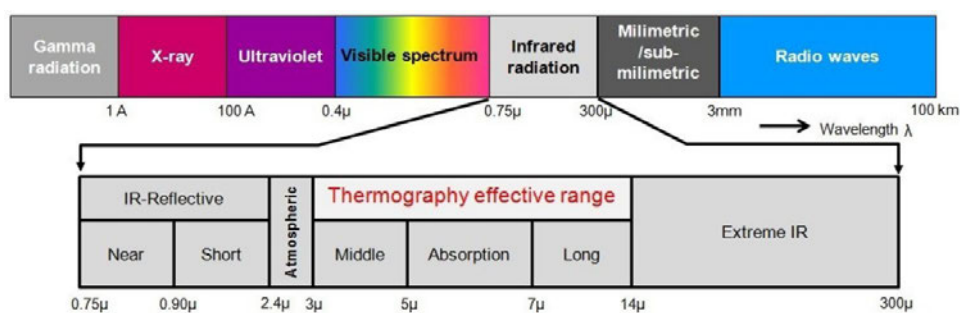


Figure 2.6: Representation of the electromagnetic spectrum and IR radiation classification and the associated wavelengths (MedIT, 2011)

The IR spectrum consists of 5 separate regions, the shortwave region from 0.75 to 3 μ m, the mid-wave region from 3 to 5 μ m, the absorption region is 5 to 7 μ m, the longwave region from 7 to 14 μ m and the extreme region from 14 to 300 μ m. For EST screening, IR cameras are operated in the longwave region. All objects

with a temperature above 0 K emit IR radiation due to the thermal motion of their molecules. The relation between energy and temperature is explained by Stefan - Boltzmann's law. Emissivity is 1 for perfect black-bodies that absorb all incident EM radiation. For grey-bodies, emissivity is less than one. Stefan-boltzmann's approximation for a grey-body is expressed in equation 2.5 [36].

$$P = \epsilon \cdot \sigma \cdot T^4 \quad (2.5)$$

here P is the total emissive power (W/m^2), σ is the stefan boltzmann's constant ($\sigma = 5.67 \times 10^{-8} \text{ W}/\text{m}^2$) and T is the object's absolute temperature in K. The spectral emission of a black body as described by planck's law is seen in equation 2.6 [37].

$$L_{\lambda}(T) = \frac{2hc^2}{\lambda^5} \frac{1}{e^{\frac{hc}{\sigma T \lambda}} - 1} \quad (2.6)$$

Here L_{λ} is the spectral radiance expressed per unit wavelength ($\text{W} \cdot \text{sr}^{-1} \cdot \text{m}^{-3}$). For temperatures below 500 K, the emission is predominantly in the IR region. The corresponding plot for different temperature peaks is represented in Fig 2.7.

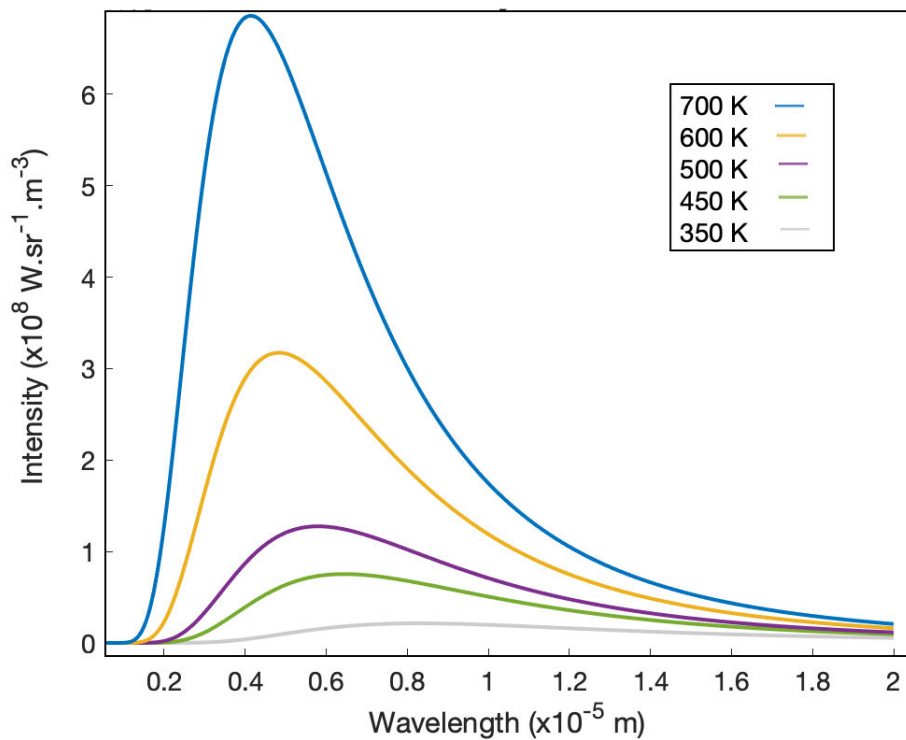


Figure 2.7: The spectral radiance or intensities at different wavelength. Different temperatures of 350 K, 450 K, 500 K, 600 K and 700 K are plotted with their intensity peaks at different temperatures. Intensity peaks for measurement of temperatures below 350 K are focused above wavelengths of 0.75 μm .

2.3.2. Heat Transfer variation with Ambient Temperature and Distance

The heat radiated between subject and camera varies with ambient temperature and distance. An illustration of the skin surface being measured by the camera is shown in figure 2.8.

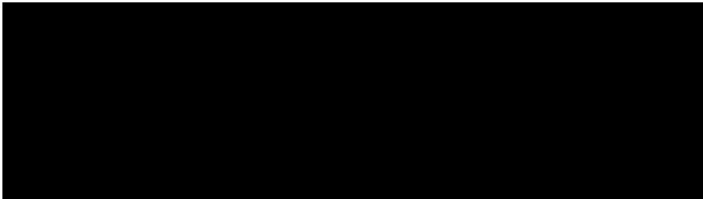
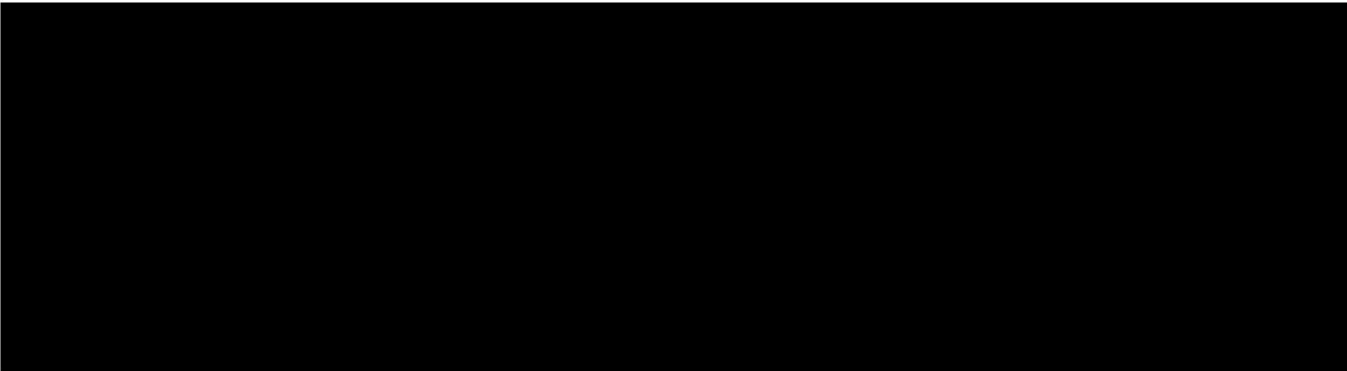
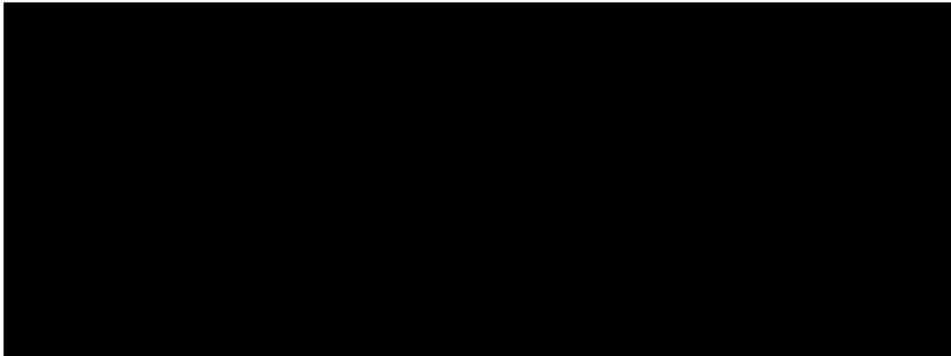


Figure 2.8: Illustration of the subject's skin surface (s) and camera's detector array (d) separated by a distance 'R'.

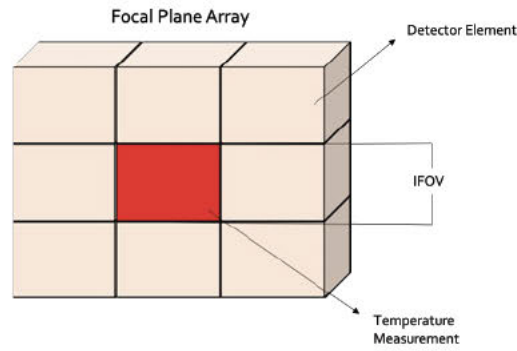


2.3.3. Camera Pixel Spatial Coverage

IR camera has a fixed sensor that provides a definite number of pixels. [Redacted]



[Redacted]



The formula for spot size calculation is shown in equation 2.8.

$$S_{cam} = I_{cam} \cdot d_{obj} \quad (2.8)$$

here S_{cam} is the area coverage size of the pixel, I_{cam} is the instantaneous field of view of the pixel and d_{obj} is the distance between the camera and the object. The spot size analysis for the FLIR A35 camera used in this setup is shown in section 3.1.2.

2.3.4. Distance Estimation using Image Information

One of the objectives of the project is to measure subjects from 0.6 m to 2 m. This could be done using an estimation of the image height. An illustration of the object and the camera is seen in figure 2.11.

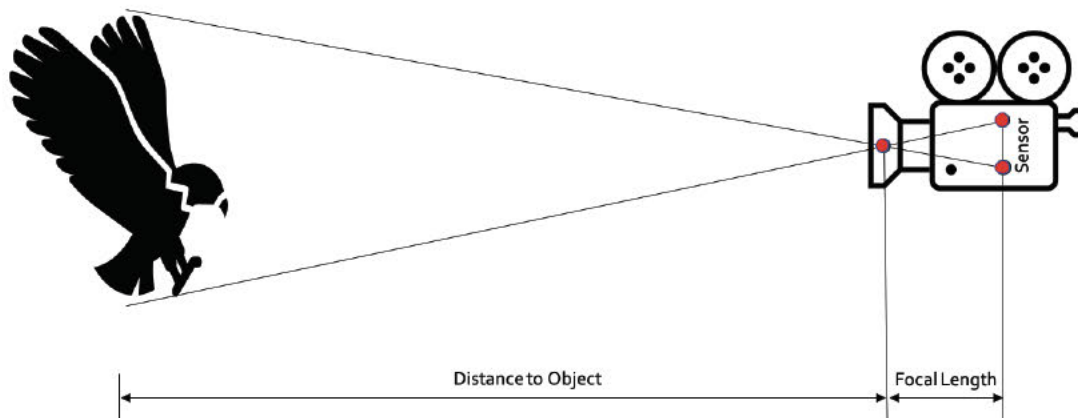


Figure 2.11: An illustration of an object at a distance from the camera. The distance of the subject to the camera is proportional to the focal length.

Using the pinhole camera model and similar properties triangle a correlation between the object's image height and distance can be made (seen in Equation 2.9) [40].

2.3.5. Signal Extraction and Filtering for Abnormal Respiration Screening

Abnormal respiration can be screened by interpretation of the visualised respiratory information or from the respiratory rate deviation. Respiratory information can be obtained by processing temperature from a suitable region of interest on the mask around the nostrils and the mouth.

Signal Extraction Technique

The average temperature from the ROI (described in section 2.2.2) is extracted using NumPy [42]. Using matplotlib in Python, the corresponding average temperature values are plotted along with the timestamps [43].

Smoothing Filter Selection

Observations during the original implementation showed the existence of a noisy signal output. For the purpose of smoothing the signal output, a filter is required. A selection of the smoothing filter was made based on the application choice. The two most popularly used filters are savitzky - golay and moving average

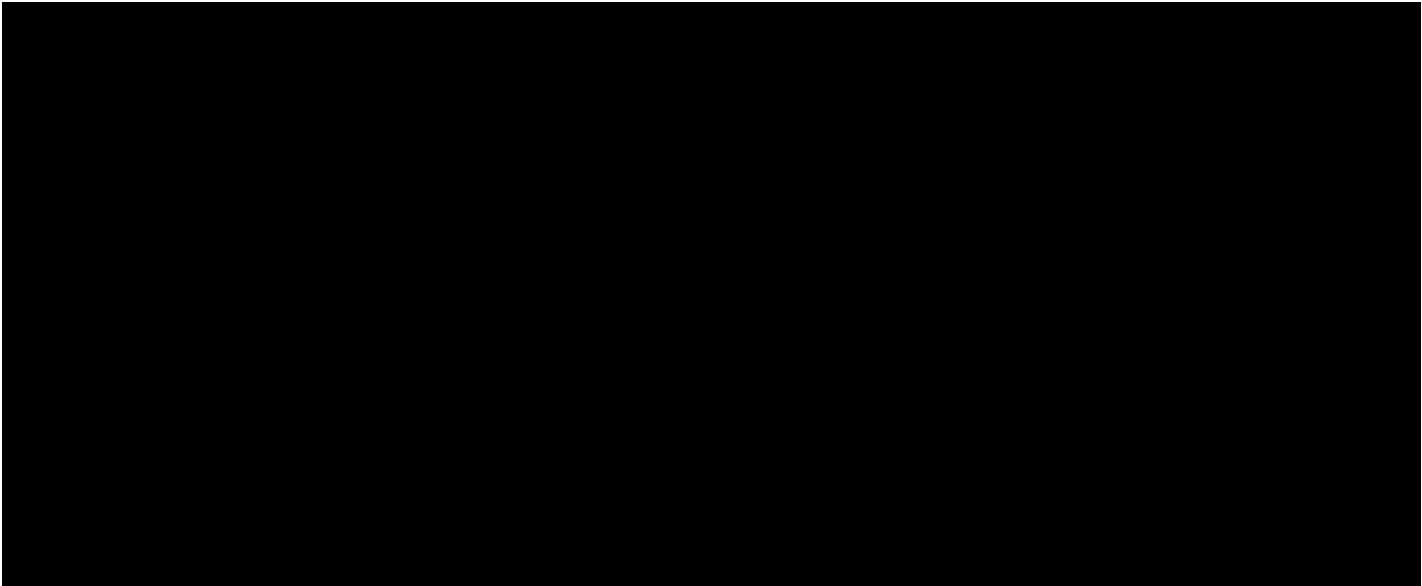


2.4. System Outline

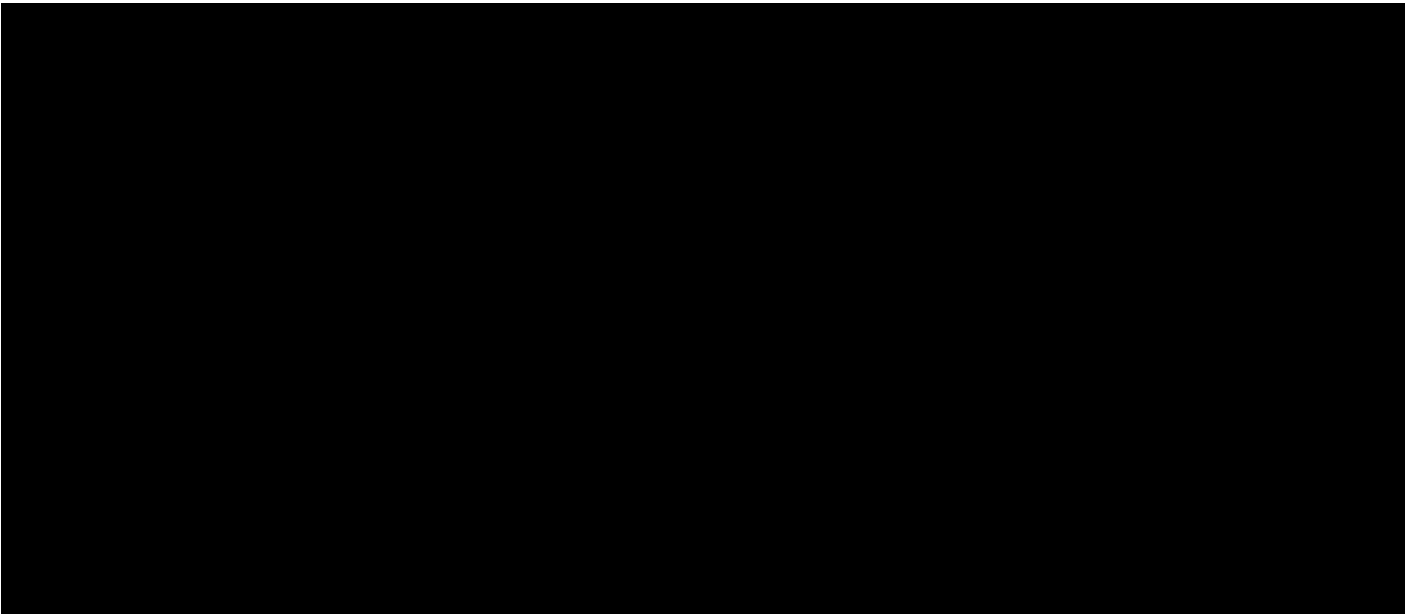
The layers are listed in the data flow order from hardware (raw information acquisition) to user display (display window for understanding vital signs). 



 A detailed overview of the system blocks are shown in figure 2.12.



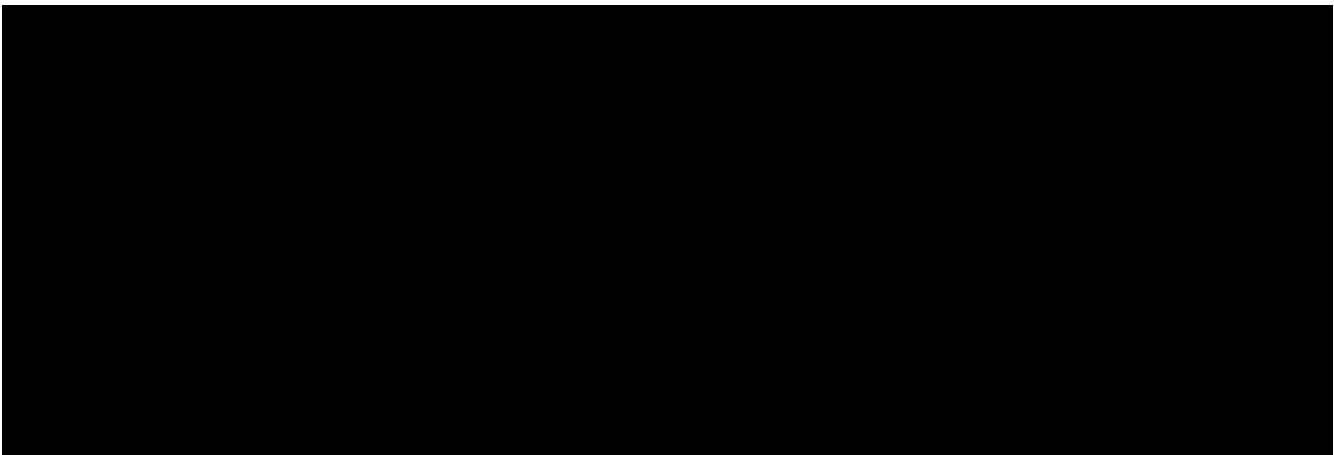
The following sections provide an overview of the different blocks used for implementation. The repositories from which the code is used in the different blocks are provided. These were used as references for implementation of individual sub-blocks in the current system (seen in figure 2.13).



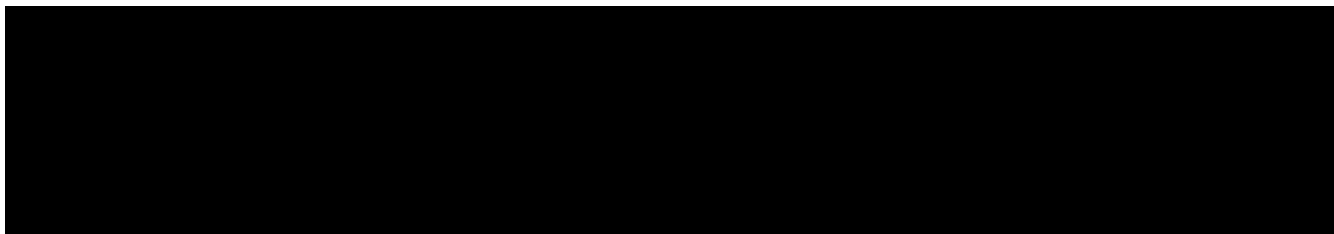
2.4.1. Hardware and Communication Interface of the System

The hardware and communication sections are combined to provide a better understanding of the data flow.

Environmental Sensor



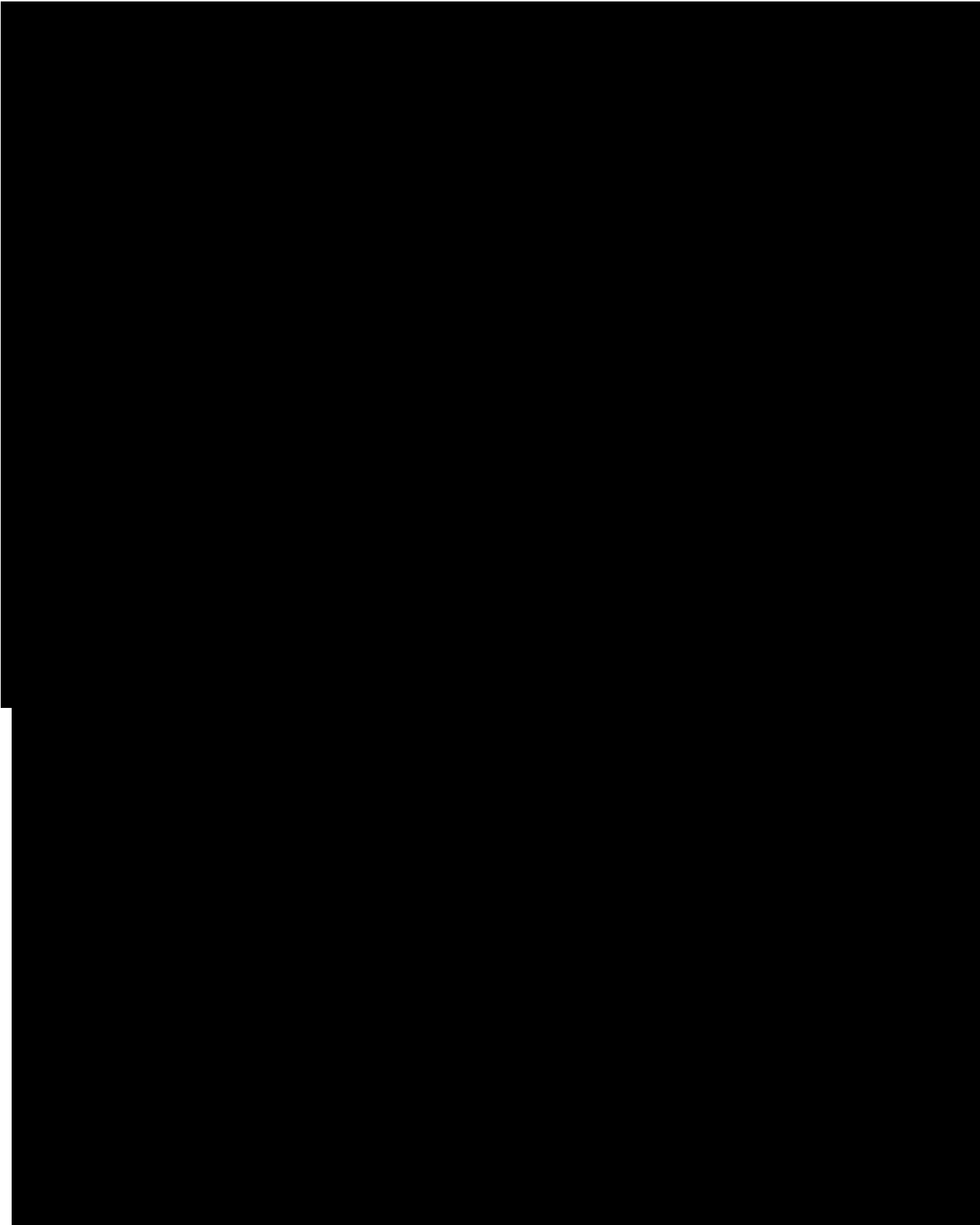
IR Camera



2.4.2. Image Processing of Thermal Camera Frames

Pre-processing from Camera

The pre-processing section explains the frame acquisition and frame conversion.



Frame Conversion

The frame conversion block involves using two functions to perform the temperature conversion and the face

detection input conversion.



Face Detection using RetinaFace

The face detection code was adapted and extended in line with the direction of the project from the github repository [54]. The Retinafacer50v1 is chosen as the most optimum face detection model. [REDACTED]

[REDACTED]

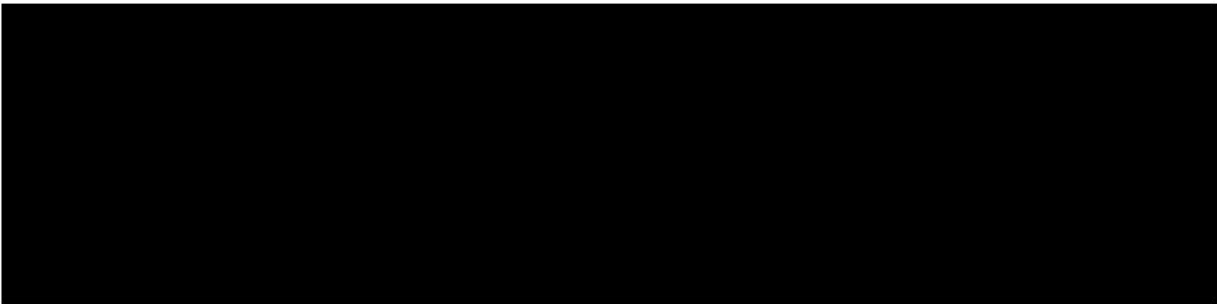
[REDACTED]

[REDACTED]

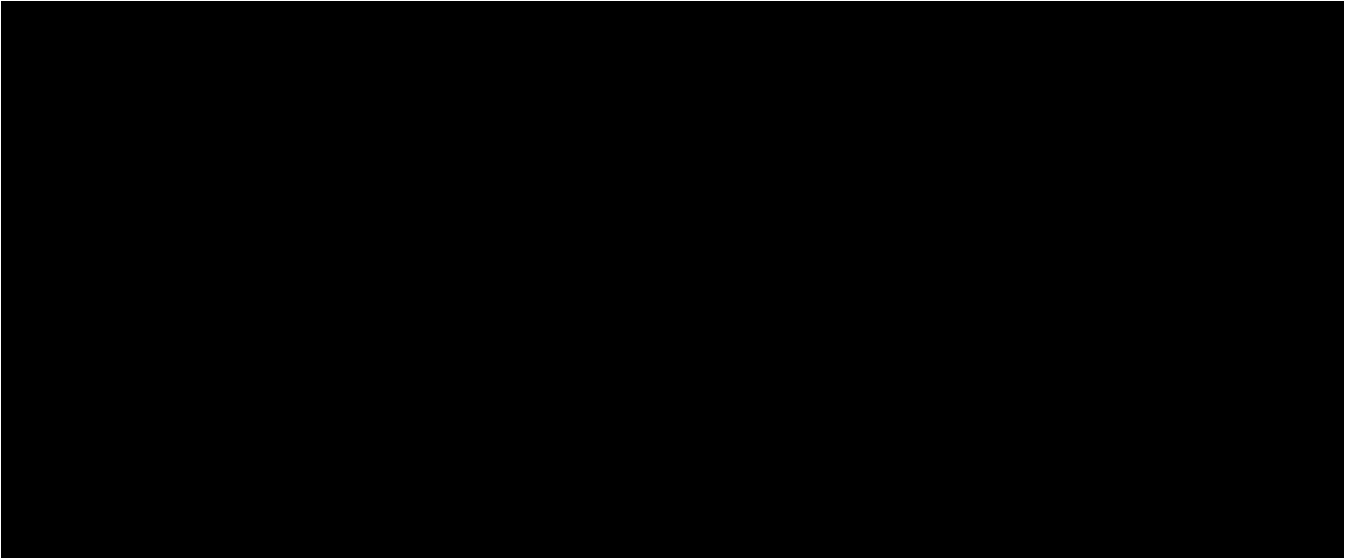
[REDACTED]

[REDACTED]

[REDACTED]

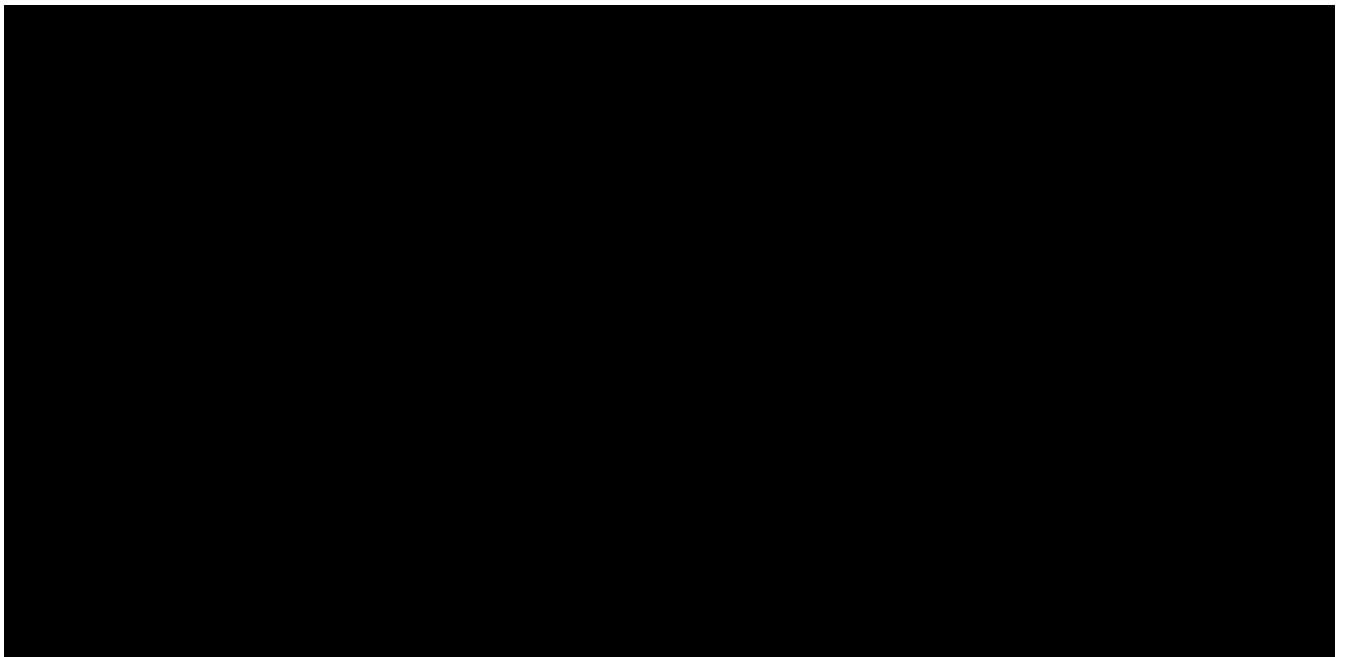


The bounding box and five landmark coordinates are used to find the different vectors. Figure 2.16 shows the retina face output of a grey-scale image.



ROI Selection

The bounding box height vector is used to segment the forehead and retrieve the temperature values within the segmented area as a 2d array. With the obtained facial bounding box information seen in figure 2.16, the next step involves establishing an optimum ROI and measurement method for temperature detection. In this approach for forehead segmentation, the goal is to segment the forehead region from the bounding box directly. The partial forehead segmentation is done by dividing the face based on a pre-fixed ratio. The coordinates from the facial bounding array are used to get the forehead location. The forehead selection methodology is illustrated in figure 2.17.



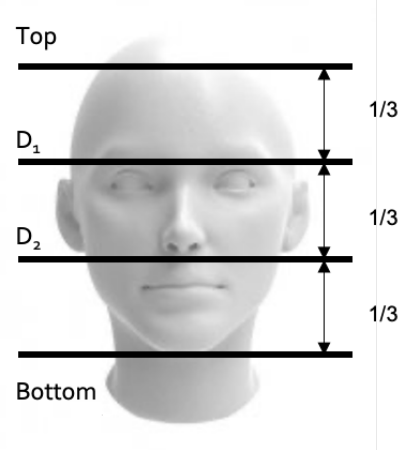
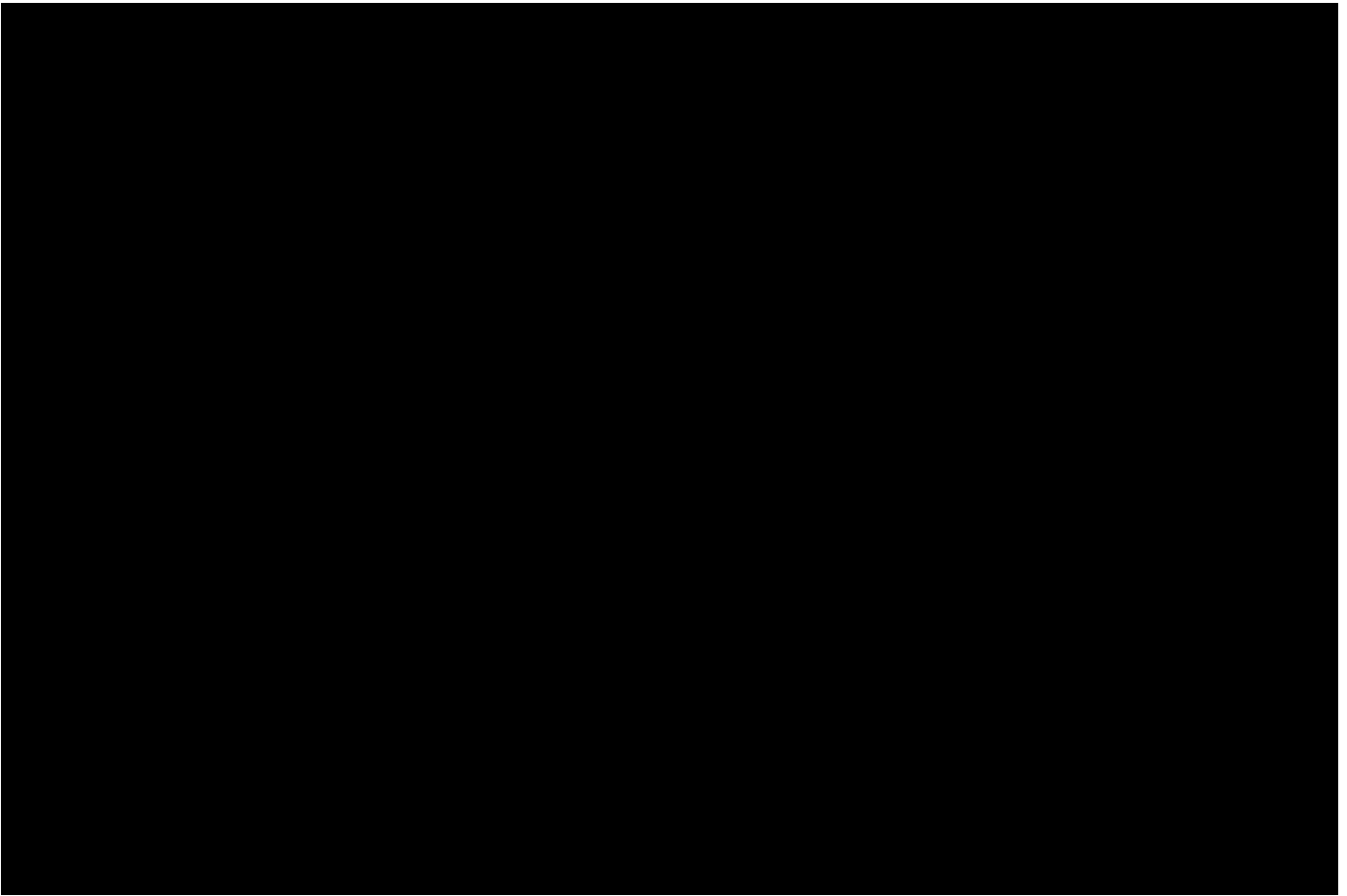


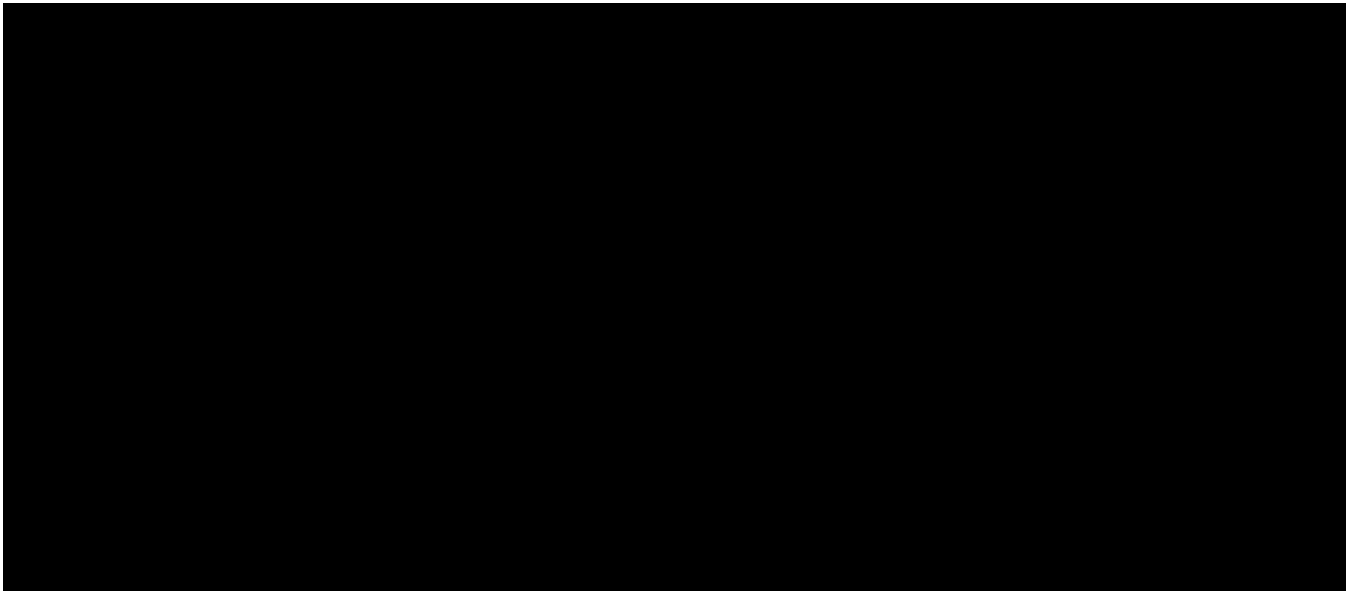
Figure 2.18: The face is generally divided equally into three portions (image adapted from [58]). The portion between the top and D₁ constitute the forehead. The portion below D₁ to the bottom constitute the remaining part of the face.

Based on figure 2.18, effective division ratio for segmenting forehead is chosen between 2 and 6 between D₂ and the top of the forehead. Segmentation with the intention that the forehead’s superficial artery areas had to be covered and that the inner canthus is to be avoided. A ranking of the different indices is done to





The corresponding visual representation of the maximum location with the exact pixel location is shown in figure 2.21.



Skin Temperature Compensation

Compensation of the acquired skin temperature can be done using the model developed in this project (section 3.3.5). 

[REDACTED]

[REDACTED]

[REDACTED]

2.5. Choice of Hardware and Software for the Prototype

Development of the prototype requires integrating hardware and software based on a comprehensive literature review.

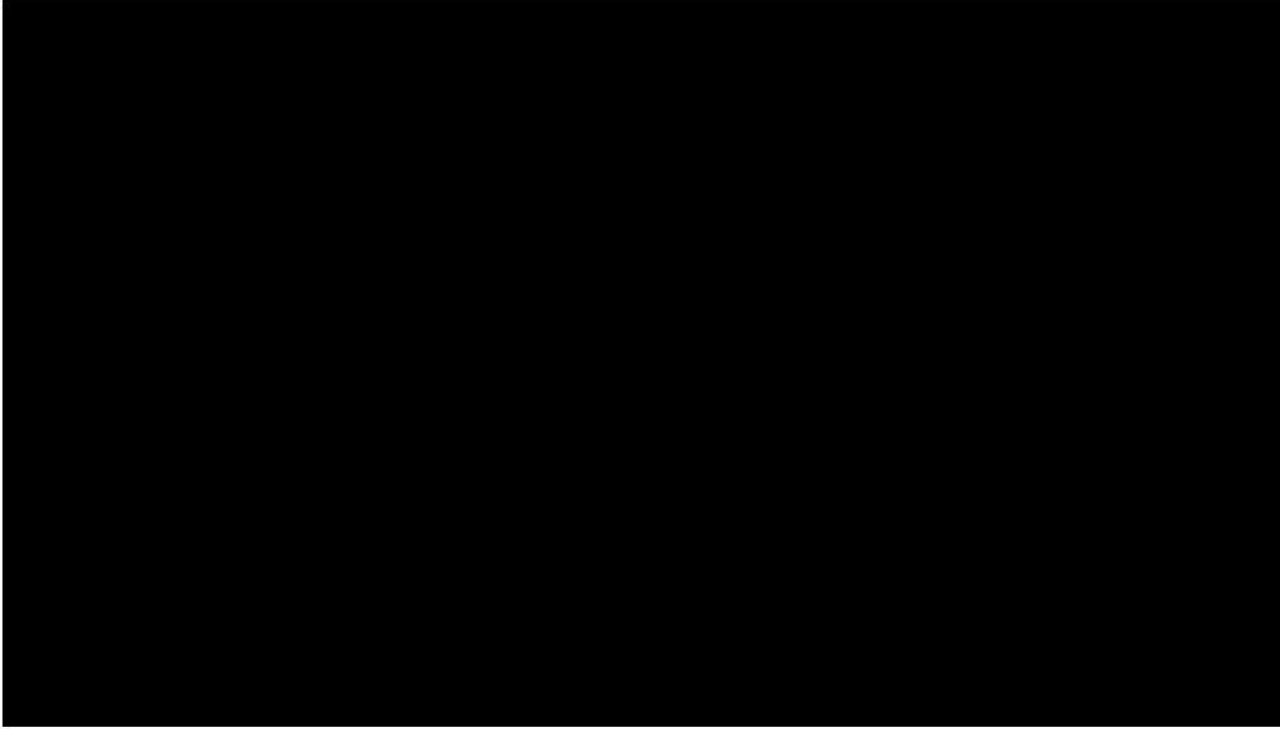
2.5.1. IR Camera Technology and Selection

IR imaging is preferred widely due to its safe and non-invasive approach. IR images are visualised photographs of the reflected, transmitted and emitted thermal radiation measured in an area [59]. Thermal imaging is highly advantageous as it gives a complete representation of the imaging area compared with point detection techniques. Selection of a suitable camera depends on cooling technology, optics, camera hardware specifications and processing techniques. Thermal cameras are expensive and have a lower resolution compared to visual cameras. IR camera resolution is generally lower than visible light imager because thermal detectors need to sense larger wavelength than visible light[39]. This makes the sensor elements quite large. A higher number of pixels (resolution) will give a relatively better quality of temperature measurement. The radiance is measured across each pixel element in the focal plane array of the camera[39]. Each pixel generates a signal that is related to the total flux per unit area [39]. A higher number of frames recorded per second (frame rate) would better readout in dynamic environments.

Accuracy of the camera is crucial in measuring skin temperature. Auto-calibration of the camera to accommodate internal temperature drift is crucial for stabilising the measured temperature in dynamic settings. The camera's intended target regions are the forehead artery regions. The pixel's spot size should be less than the intended target area to get an accurate measurement [60]. Superficial temporal artery size varies between 1.8 and 3 mm [61]. The current camera's measurement spot size is expected to be around $2.3 \pm 1.2\text{mm}$ (based

on section 2.8) at the envisioned measurement range. Moving target measurements require cameras with a faster shutter speed to remove artefacts introduced by motion blur. Having a suitable communication interface is essential to transfer images from the camera to the processor and adequately process them. It is suitable due to the size, cost and compatibility for employment in dynamic environments. It is sufficient to ensure that this camera has a large field of view (FoV) for multiple subject screening, to accommodate wide-angle screening and is small, providing portability. Some of the widely-used and recommended cameras are listed in Table 2.4.

[REDACTED]	[REDACTED]	[REDACTED]	[REDACTED]	[REDACTED]	[REDACTED]
[REDACTED]	[REDACTED]	[REDACTED]	[REDACTED]	[REDACTED]	[REDACTED]
[REDACTED]	[REDACTED]	[REDACTED]	[REDACTED]	[REDACTED]	[REDACTED]





2.5.3. Environmental Sensor, Interfacing and Supporting Equipment

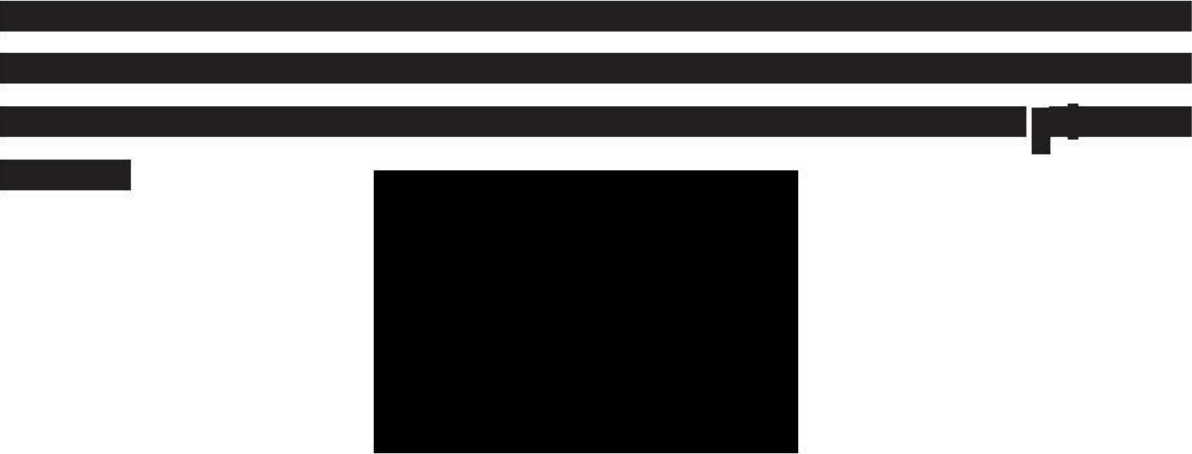
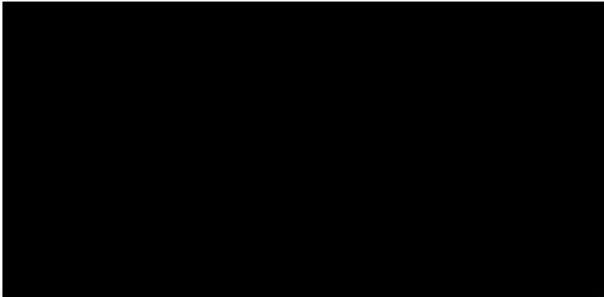


Figure 2.24: The BME 280 sensor with breakout board that is used for temperature and humidity measurement.

The specifications are highlighted in table 2.7.



[Redacted text block]

[Redacted text block]

The specifications are described in table 2.8.

[Redacted text block]

[Redacted text block]

[Redacted text block]

Table 2.9 gives an overview of the specifications.

[REDACTED]	[REDACTED]

[REDACTED]

[REDACTED]

[REDACTED]	[REDACTED]

[REDACTED] y

[REDACTED]



[REDACTED]

The specifications are highlighted in table 2.11.

[REDACTED]	[REDACTED]

[REDACTED]

Facial Bounding Box Vector Description

The bounding box coordinates that are obtained from the face detection algorithm are used to obtain the vectors. The vertices of the bounding box are explained in figure 2.28.

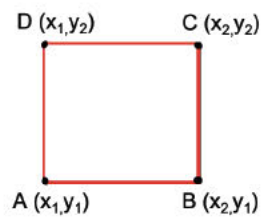


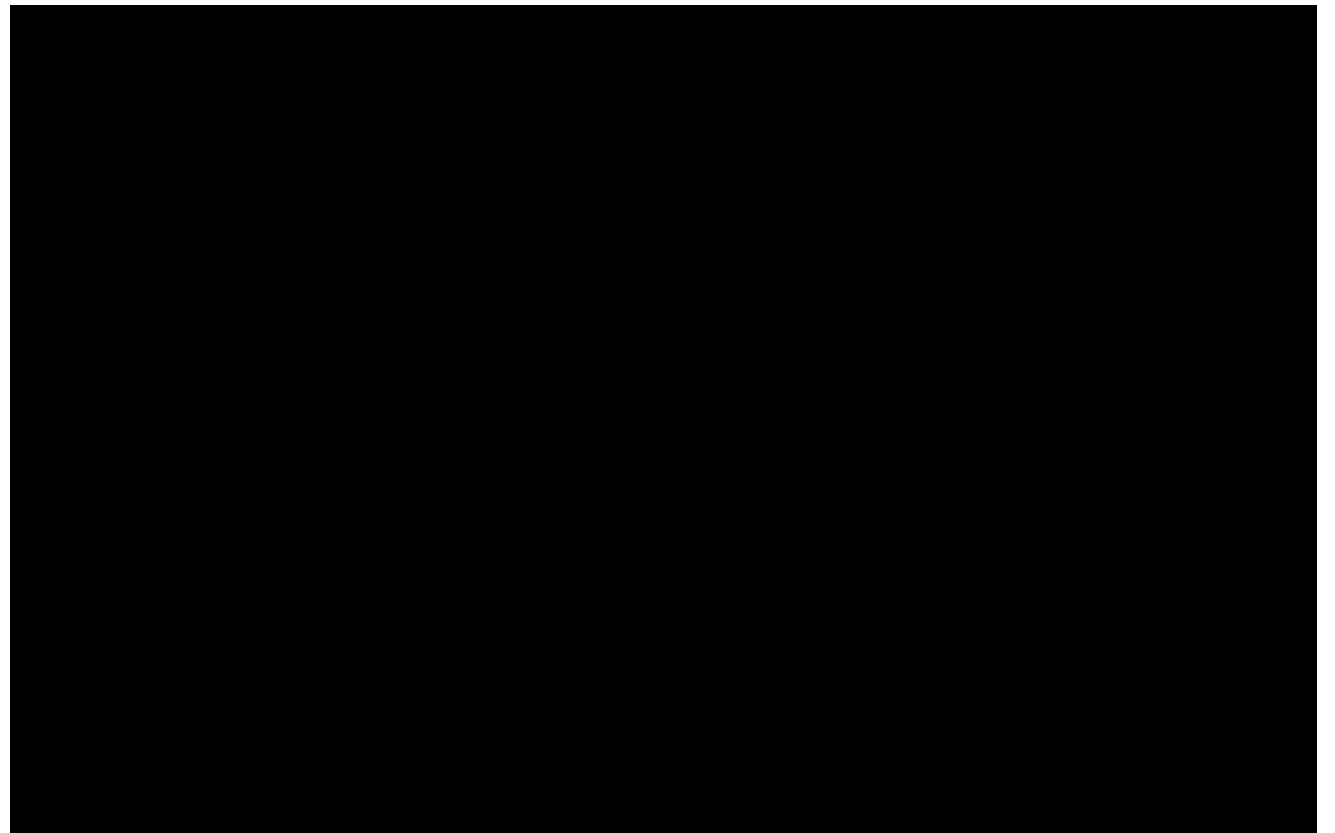
Figure 2.28: The facial bounding box vector in notation format. A(x,y), B(x,y), C(x,y) and D(x,y) are the different vertices of the bounding box vector.

The four vertices of the bounding box A, B, C and D are represented with the corresponding cartesian coordinate system. The four bounding vectors are height, width, diagonal fx and diagonal shown in figure 2.29.

[REDACTED]

[REDACTED]

[REDACTED]



2.7. Elevated Skin Temperature and Abnormal Respiration Screening

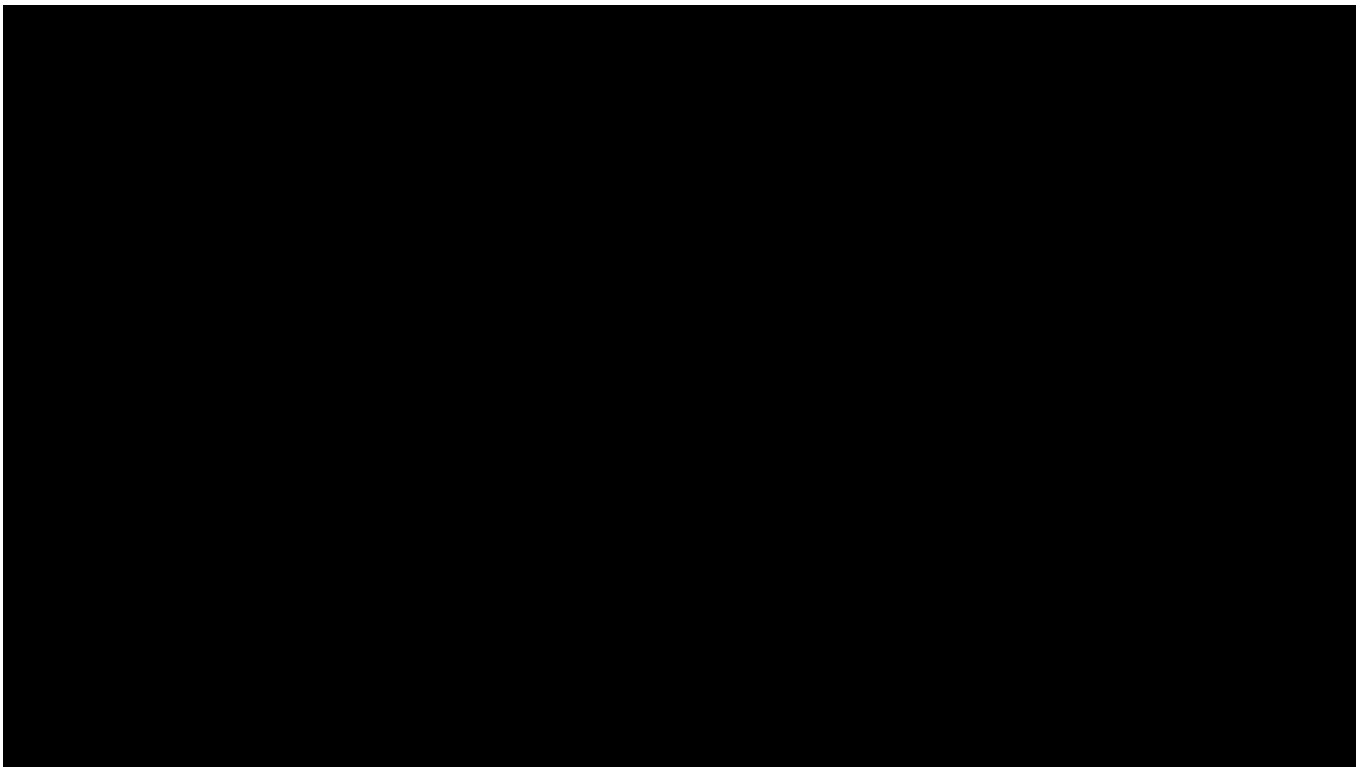
Thermal imaging systems are widely used to screen for fever at public places [72]. While COVID-19 is conclusively diagnosed by demonstrating the virus's presence in a person's respiratory secretions, the evaluation of vital signs provides valuable initial information regarding the infection in such respiratory illnesses.

EST Screening

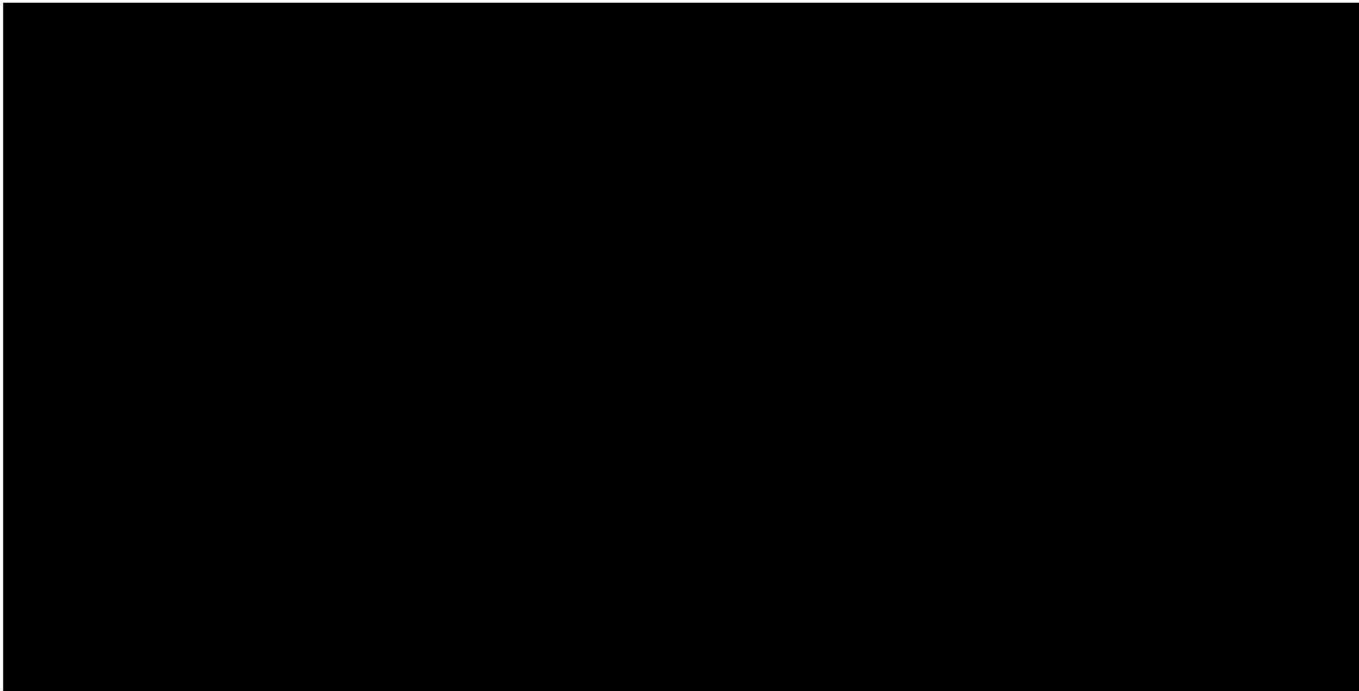
Body temperature is the oldest and most commonly measured vital sign. Abnormal body temperature is a natural indicator of illness [73]. The body temperature of an individual is maintained through their brain's

thermo-regulatory function, which creates additional heat by increasing metabolism in tissues and releases excess heat into the environment through the skin. A healthy person's core body temperature lies between 36 °C to 38 °C. Even within this normal range of human body temperature, fluctuations often occur due to the intersection of multiple individualistic and common factors including gender, age, time of year and physical activity amongst others [74]. In this project, the objective is to screen for EST by statistical comparison between different subjects. Temperature recordings above a defined threshold will indicate the possibility of a fever. Common practices for defining the threshold involve selecting it as 1 ° above the healthy temperature baseline [39]. The EST screening technique is done using a moving average filtering technique and compared against a threshold.

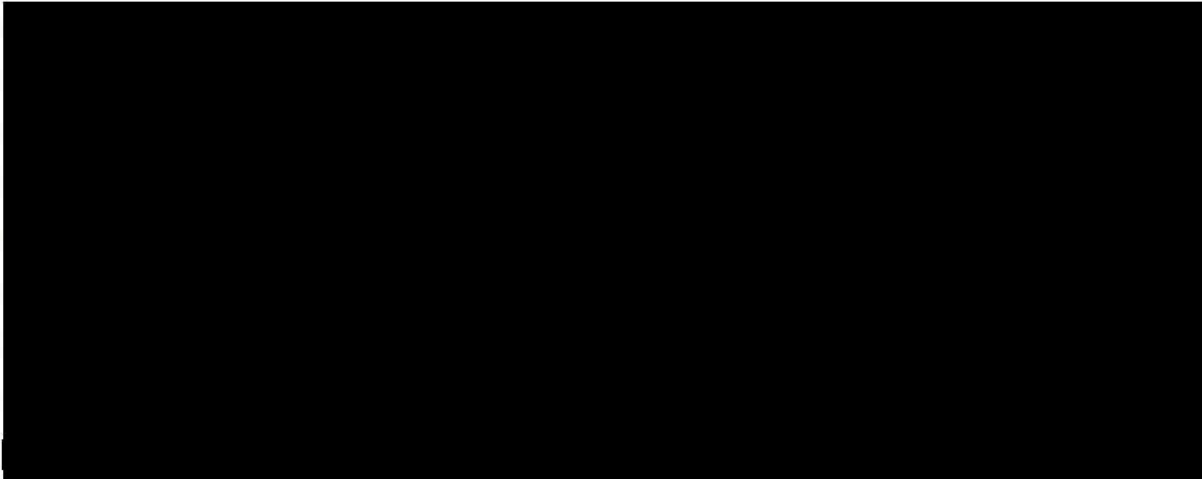
[REDACTED]



The EST screening output with a single subject is shown in figure 2.33.

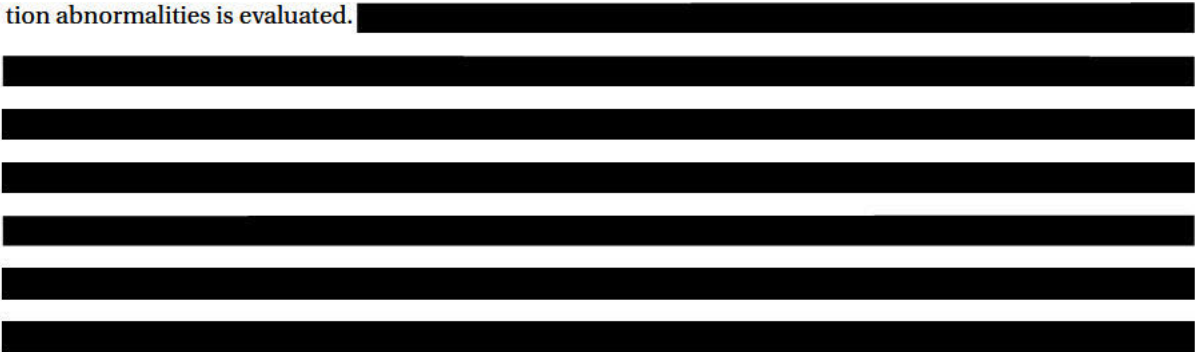


AR Screening



2.8. Chapter Conclusions

In this chapter, the requirement for screening for symptoms like elevated skin temperature (EST) and respiration abnormalities is evaluated.



[Redacted text block consisting of six horizontal bars]

3

Research, Methods and Validation

The following chapter presents the significant results in the different sections - camera calibration, image processing, distance estimation and temperature estimation. The final part of the chapter presents the validation for the different techniques and a benchmarking standard. All the frames with subject information that are used for validation are 320 x 256 pixels.

3.1. Camera Specific Procedures

3.1.1. Camera Accuracy

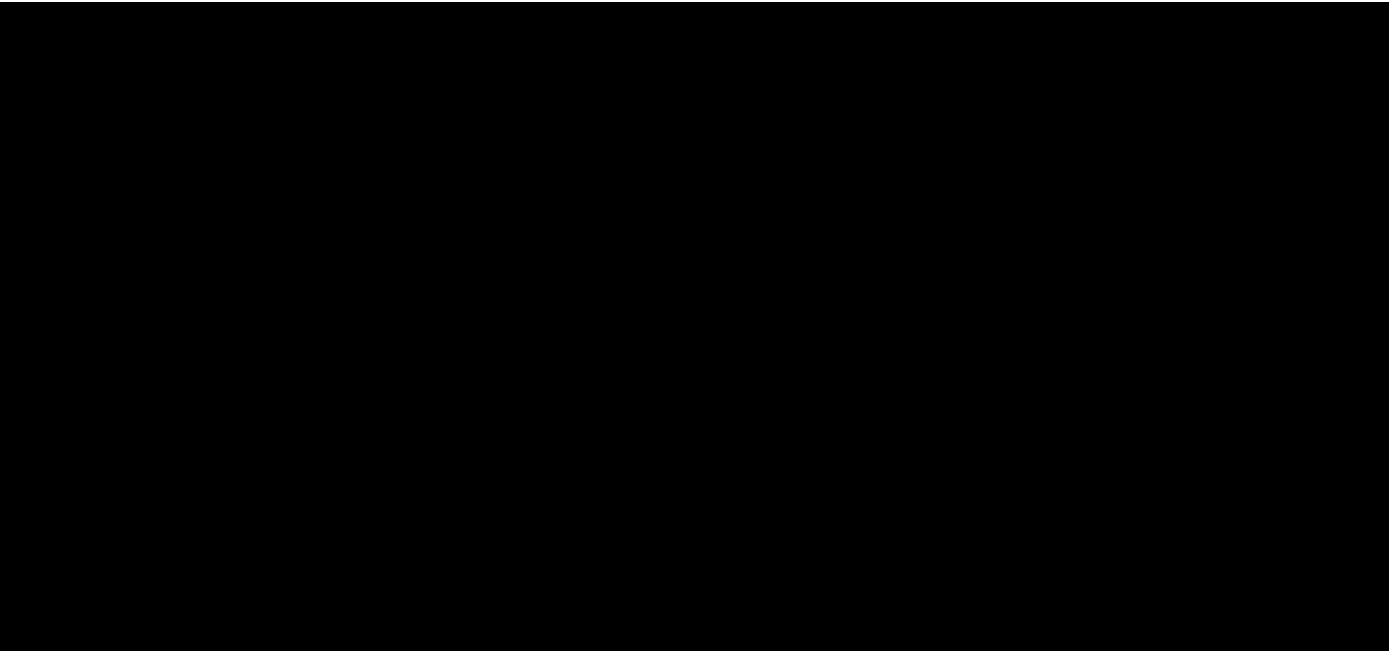
[REDACTED]



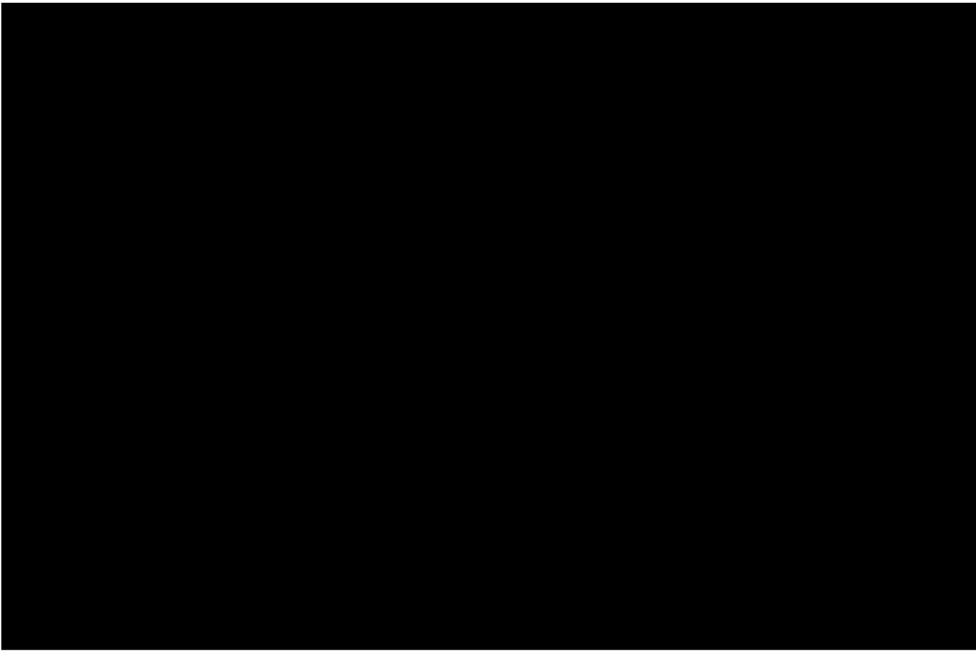
3.3. Distance and Temperature Estimation

Distance estimation is done using the facial image information of the subject (explained in sections 3.3.1 and 3.3.2). The development of the temperature compensation model is shown in section 3.3.5.

3.3.1. Modelling of Distance and Experiments



[Redacted]



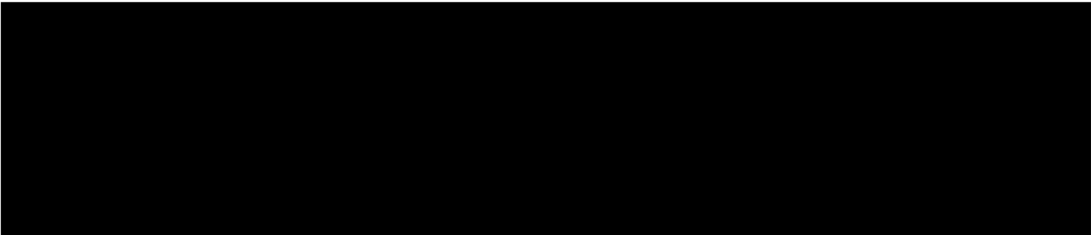
[Redacted]

3.3.5. Adaptive Temperature Compensation Model using Slope Calculation

[Redacted]

Model Inputs

[Redacted]



[Redacted]

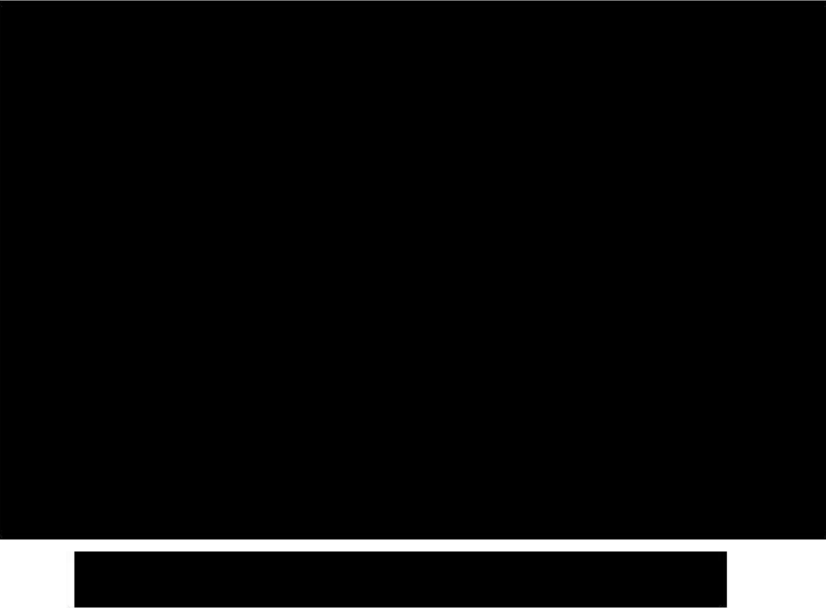
Model Input - Slope ($S_{T_{amb}}$) extraction from ambient temperature (T_{amb}) [Redacted]

[Redacted]

Model Input - Distance (d_{obj}) from object's image height [redacted]
[redacted]

Model Input - Measured skin temperature (T_{obj}) from forehead max algorithm [redacted]
[redacted]
[redacted]

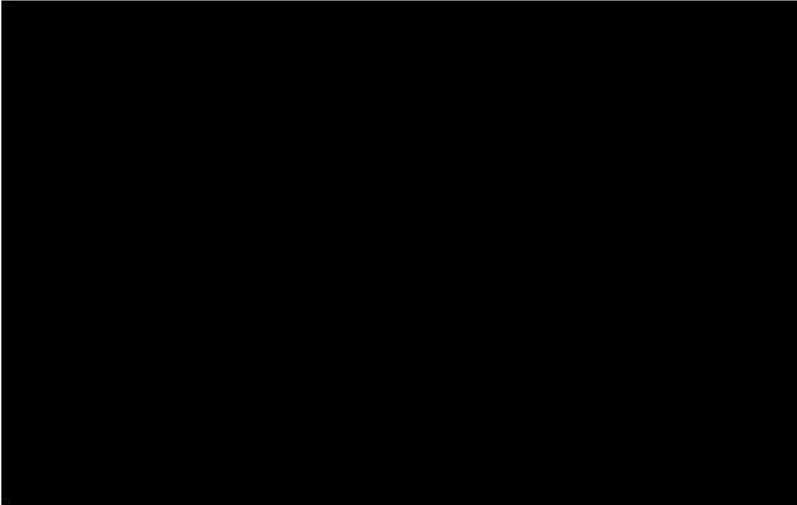
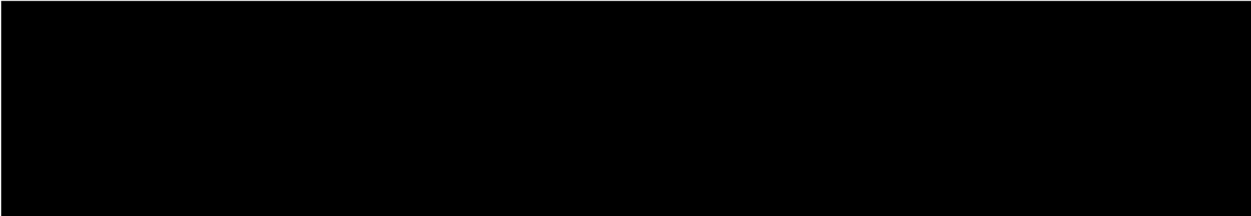
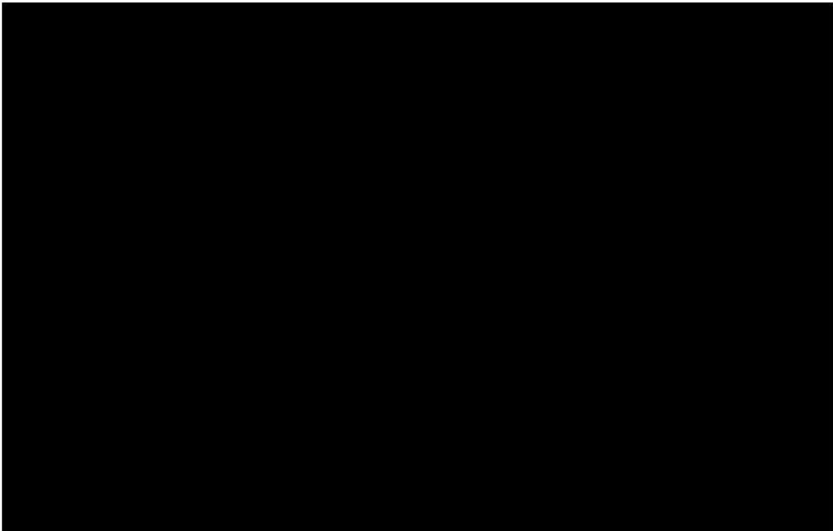
Figure 3.11 shows an illustration of the model intended to describe the adaptive compensation technique.



[redacted]
[redacted]
[redacted]
[redacted]

[redacted]

[redacted]
[redacted]



3.5. Validation

3.5.1. Region of Interest for Elevated Skin Temperature Screening

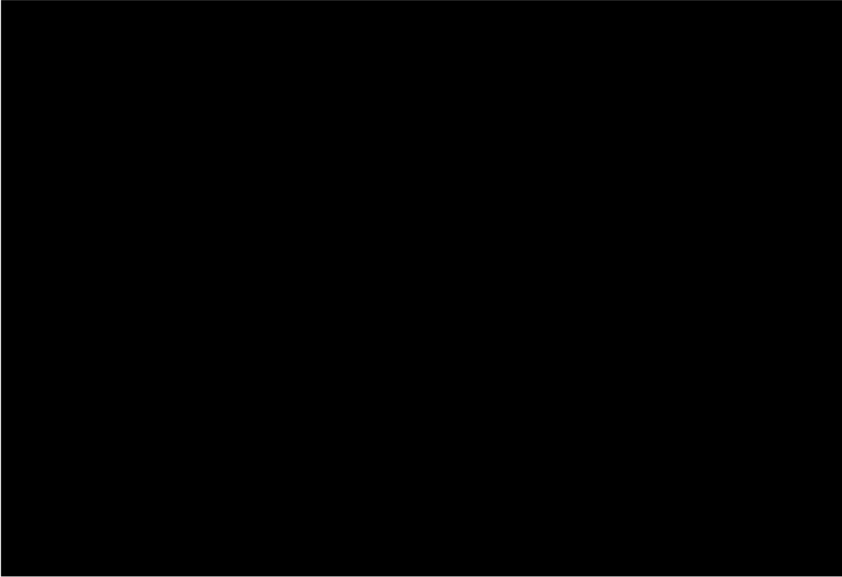
Forehead Segmentation Comparison between Different Faces

[Redacted text block]



[Redacted text line]

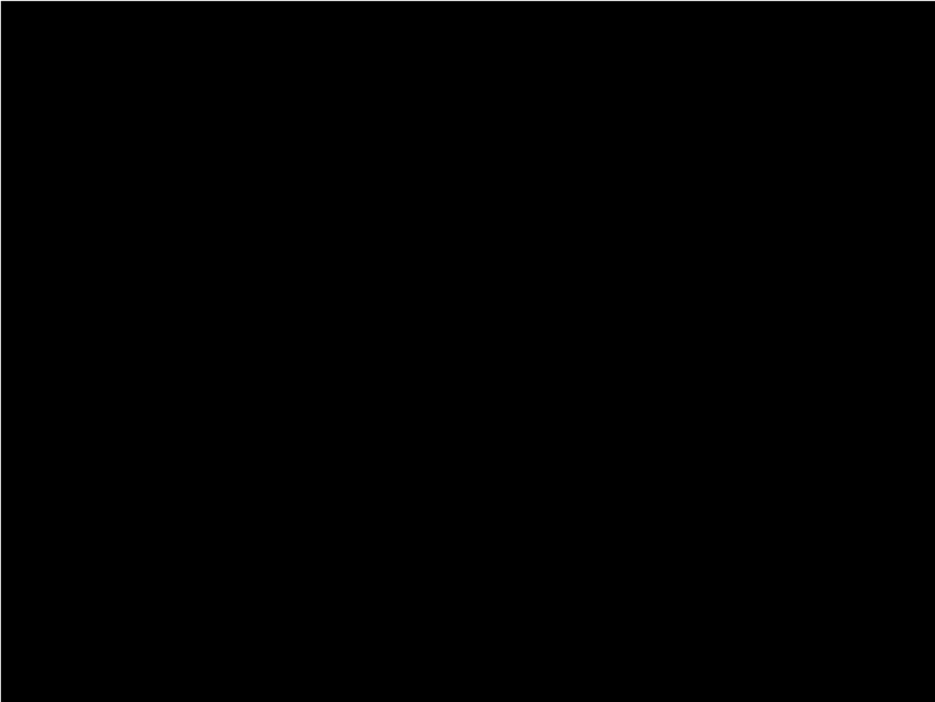
[Redacted text block]



[Redacted text line]

Location Index for temperature measurement

[Redacted text block]



[Redacted text block]

[Redacted]

3.5.3. Temperature Compensation Model

[Redacted text block]

[Redacted]

[Redacted]

[Redacted]

[Redacted]

[Redacted]

[Redacted]

[Redacted]

4

Conclusions and Future work

The following chapter consists of two different sections that outline the conclusions and future work.

4.1. Conclusions

[Redacted text block containing multiple lines of blacked-out content]

[Redacted text block]

[Redacted text block]

4.2. Future work

The future work that can be done to improve the current prototype is explained in the following subsections.

[Redacted text block]

[Redacted text block]

[Redacted text block]

[Redacted]

A

Appendix

A.1. General Requirements

The project's general requirement involves developing an IR thermal imaging system that can be used as a screening aid for clinicians. To better understand the requirements, they are segmented into two categories - physiological and technological requirements. The physiological requirements indicate the goals from a clinical perspective, and the technological requirement gives a system requirement perspective. [REDACTED]

[REDACTED]

[REDACTED]

[REDACTED] The list of requirements is described using MoSCoW analysis in section A.2.

A.2. Project Requirement Analysis

Functional requirements provide an overview of the physiological and technological implementations that are essential to the system. Non-functional requirements include other specifics to enhance the system.

A.2.1. Functional Requirements

[REDACTED]

[REDACTED]



Would have:



A.2.2. Non-Functional Requirements

This deals with the implementation platform of the system.

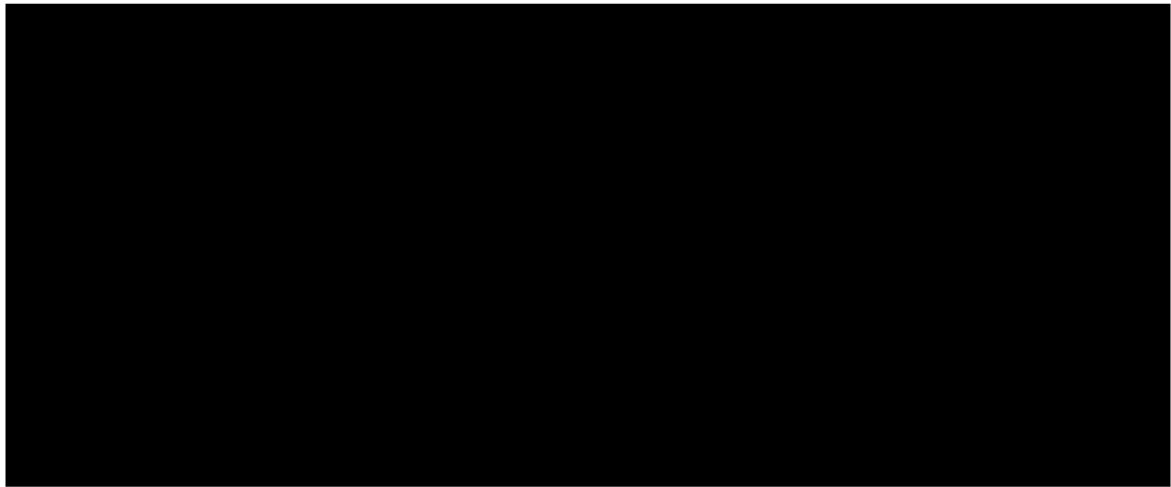
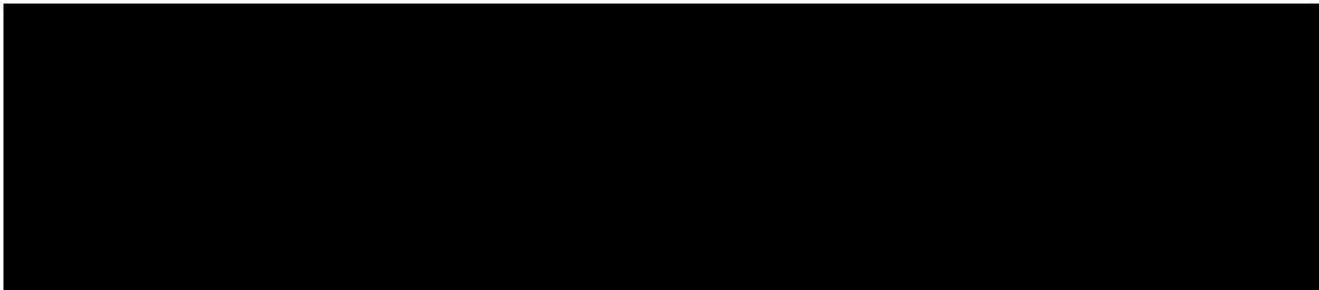
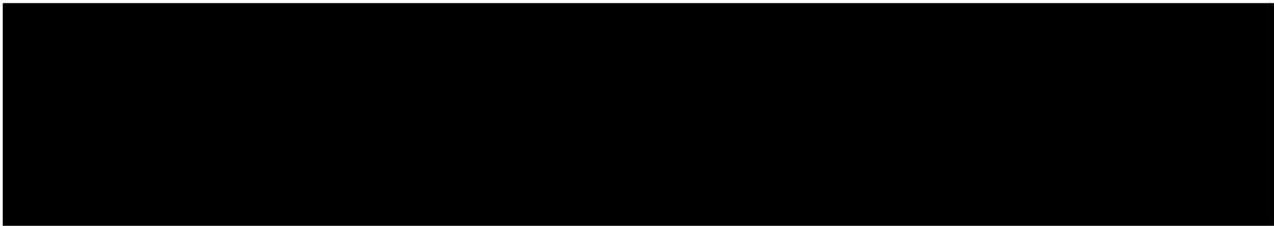


Figure A.1: Illustration of the top and side view of the camera with a extended representation of the field of view

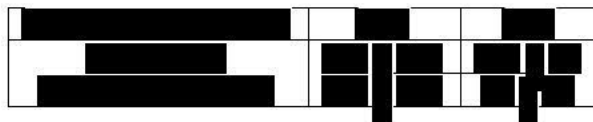
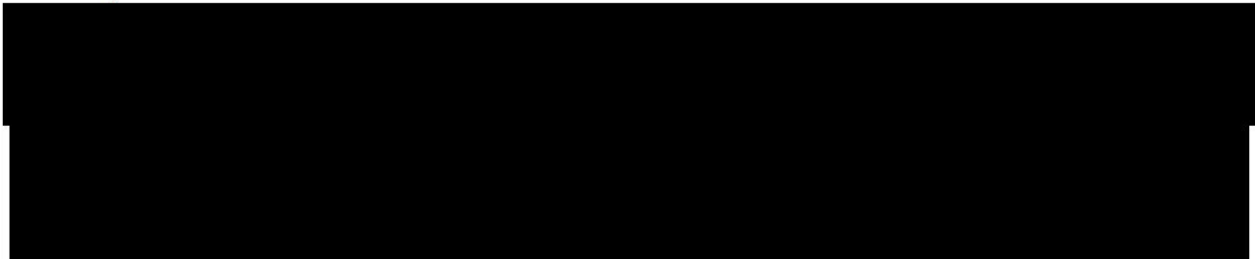
The corresponding horizontal distance measurements can be explained by equation A.2



here e_1 is extended distance (x-direction).



A.4. System Run Time



A.5. Ethical Considerations

For experimentation, the necessary consent and permissions have been obtained (attached below).

[REDACTED]	
[REDACTED]	■
[REDACTED]	■
[REDACTED]	■
[REDACTED]	
[REDACTED]	■

List of Abbreviations

API	Application Programming Interface
AR	Abnormal Respiration
CDC	Centers for Disease Control and Prevention
CNN	Convolutional Neural Network
COVID-19	Coronavirus disease 2019
CPU	Central Processing Unit
CUDA	Compute Unified Device Architecture
CV	Computer Vision
DL	Deep Learning
DNN	Dynamic Neural Network
EST	Elevated Skin Temperature
FoV	Field of View
GenICam	Generic Interface for Cameras
GigE	Gigabit Ethernet
GPU	Graphics Processing Unit
HCW	Health care worker
IFOV	Instantaneous field of view
IoU	Intersection of Union
IR	Infrared
IRT	Infrared Thermography
MERS	Middle-East Respiratory Syndrome

ML	Machine Learning
NMS	Non-maximum supression threshold
OpenCV	Open source computer vision library
PoE	Power over Ethernet
RGB	Red, Green and Blue
RH	Relative Humidity
ROI	Region of Interest
RoM	Range of Motion
RR	Respiratory Rate
SARS	Severe Acute Respiratory Syndrome
SARS-CoV-2	Severe Acute Respiratory Syndrome Corona Virus 2
SDK	Software Development Kit
WHO	World Health Organisation

List of Symbols

n_{rate}	Net rate of heat transfer by radiation
ϵ	Emissivity
A	Surface area
σ	Boltzmann constant
T_{skin}	Skin temperature
T_{amb}	Ambient temperature
Q_{conv}	Convective heat transfer
k	Heat transfer coefficient
A_{nasal}	Internal surface area of nose
T_{nasal}	Inner nasal temperature
Q_{rad}	Radiated heat at nostrils
A_c	Area of nose
T_{nose}	Nose Temperature
H_B	Height of bounding box vector
W_B	Width of bounding box vector
D_B	Diagonal of bounding box vector
\dot{D}_B	Diagonal fx of bounding box vector
E	Energy of the photon
h	Planck constant
f	Frequency of the wave
c	Velocity of light

λ	Wavelength
P	Total emissive power
T	Object's absolute temperature in K
L_λ	Spectral radiance per unit wavelength
S	Skin surface of subject
D	Detector array of camera
R	Distance of object from camera
ϵ	Emittance
ϵ_λ	Spectral emittance
$\epsilon_{\lambda, T}$	Spectral emittance at temperature T
$\epsilon_{\lambda, T, \text{skin}}$	Spectral emittance of skin at temperature T
$\epsilon_{\lambda, T, \text{skin}, \text{max}}$	Maximum spectral emittance of skin at temperature T
$\epsilon_{\lambda, T, \text{skin}, \text{min}}$	Minimum spectral emittance of skin at temperature T
$\epsilon_{\lambda, T, \text{skin}, \text{avg}}$	Average spectral emittance of skin at temperature T
$\epsilon_{\lambda, T, \text{skin}, \text{eff}}$	Effective spectral emittance of skin at temperature T
$\epsilon_{\lambda, T, \text{skin}, \text{eff}, \text{max}}$	Maximum effective spectral emittance of skin at temperature T
$\epsilon_{\lambda, T, \text{skin}, \text{eff}, \text{min}}$	Minimum effective spectral emittance of skin at temperature T
$\epsilon_{\lambda, T, \text{skin}, \text{eff}, \text{avg}}$	Average effective spectral emittance of skin at temperature T
$\epsilon_{\lambda, T, \text{skin}, \text{eff}, \text{max}, \text{min}}$	Range of maximum and minimum effective spectral emittance of skin at temperature T
$\epsilon_{\lambda, T, \text{skin}, \text{eff}, \text{max}, \text{min}, \text{avg}}$	Average of maximum and minimum effective spectral emittance of skin at temperature T
$\epsilon_{\lambda, T, \text{skin}, \text{eff}, \text{max}, \text{min}, \text{avg}, \text{max}}$	Maximum of average of maximum and minimum effective spectral emittance of skin at temperature T
$\epsilon_{\lambda, T, \text{skin}, \text{eff}, \text{max}, \text{min}, \text{avg}, \text{min}}$	Minimum of average of maximum and minimum effective spectral emittance of skin at temperature T
$\epsilon_{\lambda, T, \text{skin}, \text{eff}, \text{max}, \text{min}, \text{avg}, \text{max}, \text{min}}$	Range of maximum and minimum of average of maximum and minimum effective spectral emittance of skin at temperature T

Bibliography

- [1] P. R. Chai, F. Z. Dadabhoy, H.-W. Huang, J. N. Chu, A. Feng, H. M. Le, J. Collins, M. Da Silva, M. Raibert, C. Hur *et al.*, “Mobile robotic systems in patient-facing functions: national acceptability survey, single site feasibility study and cost-effectiveness analysis,” *medRxiv*, 2020.
- [2] L. Rivett, S. Sridhar, D. Sparkes, M. Routledge, N. K. Jones, S. Forrest, J. Young, J. Pereira-Dias, W. L. Hamilton, M. Ferris *et al.*, “Screening of healthcare workers for sars-cov-2 highlights the role of asymptomatic carriage in covid-19 transmission,” *Elife*, vol. 9, p. e58728, 2020.
- [3] W. E. Saltzstein, M. Sabri, A. P. Dobaj, and E. O. Baumann, “Medical patient vital signs-monitoring apparatus,” Aug. 3 1999, uS Patent 5,931,791.
- [4] W. H. Organization *et al.*, “Clinical management of severe acute respiratory infection (sari) when covid-19 disease is suspected: interim guidance, 13 march 2020,” World Health Organization, Tech. Rep., 2020.
- [5] L. H. Nguyen, D. A. Drew, M. S. Graham, A. D. Joshi, C.-G. Guo, W. Ma, R. S. Mehta, E. T. Warner, D. R. Sikavi, C.-H. Lo *et al.*, “Risk of covid-19 among front-line health-care workers and the general community: a prospective cohort study,” *The Lancet Public Health*, vol. 5, no. 9, pp. e475–e483, 2020.
- [6] G. Fitbit and Apple, “Fitbit, Garmin and Apple,” <https://www.fitbit.com/global/us/home>, <https://www.garmin.com/en-US/>, Fitbit, Garmin and Apple.
- [7] D. Teichmann, C. Brüser, B. Eilebrecht, A. Abbas, N. Blank, and S. Leonhardt, “Non-contact monitoring techniques-principles and applications,” pp. 1302–1305, 2012.
- [8] A. S. Shah, R. Wood, C. Gribben, D. Caldwell, J. Bishop, A. Weir, S. Kennedy, M. Reid, A. Smith-Palmer, D. Goldberg *et al.*, “Risk of hospital admission with coronavirus disease 2019 in healthcare workers and their households: nationwide linkage cohort study,” *bmj*, vol. 371, 2020.
- [9] Y. Houdas and E. Ring, *Human body temperature: its measurement and regulation*. Springer Science & Business Media, 2013.
- [10] P. Webb, “The physiology of heat regulation,” *American Journal of Physiology-Regulatory, Integrative and Comparative Physiology*, vol. 268, no. 4, pp. R838–R850, 1995.

- [11] Z.-S. Deng and J. Liu, "Analytical study on bioheat transfer problems with spatial or transient heating on skin surface or inside biological bodies," *J. Biomech. Eng.*, vol. 124, no. 6, pp. 638–649, 2002.
- [12] J. Bouwstra and P. Honeywell-Nguyen, "Skin structure and mode of action of vesicles," *Advanced drug delivery reviews*, vol. 54, pp. S41–S55, 2002.
- [13] A. Yates, "Incontinence-associated dermatitis 1: risk factors for skin damage," *Nursing Times*, vol. 116, no. 3, pp. 46–50, 2020.
- [14] A. Coccarelli, E. Boileau, D. Parthimos, and P. Nithiarasu, "An advanced computational bioheat transfer model for a human body with an embedded systemic circulation," *Biomechanics and modeling in mechanobiology*, vol. 15, no. 5, pp. 1173–1190, 2016.
- [15] J. D. Hardy and E. F. DuBois, "Regulation of heat loss from the human body," *Proceedings of the National Academy of Sciences of the United States of America*, vol. 23, no. 12, p. 624, 1937.
- [16] M. F. Modest, *Radiative heat transfer*. Academic press, 2013.
- [17] F. J. Sanchez-Marin, S. Calixto-Carrera, and C. Villaseñor-Mora, "Novel approach to assess the emissivity of the human skin," *Journal of Biomedical Optics*, vol. 14, no. 2, p. 024006, 2009.
- [18] T. Togawa, "Non-contact skin emissivity: measurement from reflectance using step change in ambient radiation temperature," *Clinical Physics and Physiological Measurement*, vol. 10, no. 1, p. 39, 1989.
- [19] A. Boylan, C. Martin, and G. Gardner, "Infrared emissivity of burn wounds," *Clinical Physics and Physiological Measurement*, vol. 13, no. 2, p. 125, 1992.
- [20] E. Ring, "Quantitative thermal imaging," *Clinical Physics and Physiological Measurement*, vol. 11, no. 4A, p. 87, 1990.
- [21] D. S. Haddad, M. L. Brioschi, M. G. Baladi, and E. S. Arita, "A new evaluation of heat distribution on facial skin surface by infrared thermography," *Dentomaxillofacial Radiology*, vol. 45, no. 4, p. 20150264, 2016.
- [22] R. S. Erickson and T. M. Woo, "Accuracy of infrared ear thermometry and traditional temperature methods in young children." *Heart & lung: the journal of critical care*, vol. 23, no. 3, pp. 181–195, 1994.
- [23] C. B. Mogensen, L. Wittenhoff, G. Fruerhøj, and S. Hansen, "Forehead or ear temperature measurement cannot replace rectal measurements, except for screening purposes," *BMC pediatrics*, vol. 18, no. 1, p. 15, 2018.
- [24] R. B. Barnes, "Determination of body temperature by infrared emission," *Journal of applied physiology*, vol. 22, no. 6, pp. 1143–1146, 1967.

- [25] L.-S. Chan, G. T. Cheung, I. J. Lauder, and C. R. Kumana, "Screening for fever by remote-sensing infrared thermographic camera," *Journal of travel medicine*, vol. 11, no. 5, pp. 273–279, 2004.
- [26] F. Pompei, "Temporal artery temperature detector," Sep. 18 2001, uS Patent 6,292,685.
- [27] D. Sandlin, "New product review: temporal artery thermometry," *Journal of PeriAnesthesia Nursing*, vol. 18, no. 6, pp. 419–421, 2003.
- [28] J. Pankratz, J. Baer, C. Mayer, V. Rana, R. Stephens, L. Segars, and C. C. Surek, "Depth transitions of the frontal branch of the facial nerve implications in smas rhytidectomy," *JPRAS Open*, 2020.
- [29] T. von Arx, K. Tamura, O. Yukiya, and S. Lozanoff, "The face—a vascular perspective. a literature review," *Swiss dental journal*, vol. 128, no. 5, pp. 382–392, 2018.
- [30] A. K. Abbas, K. Heimann, K. Jergus, T. Orlikowsky, and S. Leonhardt, "Neonatal non-contact respiratory monitoring based on real-time infrared thermography," *Biomedical engineering online*, vol. 10, no. 1, p. 93, 2011.
- [31] S. Kakaç, R. K. Shah, and W. Aung, "Handbook of single-phase convective heat transfer," 1987.
- [32] X. Zheng, Q. Lei, R. Yao, Y. Gong, and Q. Yin, "Image segmentation based on adaptive k-means algorithm," *EURASIP Journal on Image and Video Processing*, vol. 2018, no. 1, p. 68, 2018.
- [33] M. A. Heald and J. B. Marion, *Classical electromagnetic radiation*. Courier Corporation, 2012.
- [34] E. K. ABU-DANSO, "Dissertations in forestry and natural sciences."
- [35] C. Honsberg and S. Bowden, "Photovoltaic education network," *PVEducation.org* [accessed 7 August 2015]. <http://www.pveducation.org>, 2013.
- [36] I. Montvay and E. Pietarinen, "The stefan-boltzmann law at high temperature for the gluon gas," *Physics Letters B*, vol. 110, no. 2, pp. 148–154, 1982.
- [37] D. Lawson, "A closer look at planck's blackbody equation," *Physics Education*, vol. 32, no. 5, p. 321, 1997.
- [40] K. M. Dawson-Howe and D. Vernon, "Simple pinhole camera calibration," *International Journal of Imaging Systems and Technology*, vol. 5, no. 1, pp. 1–6, 1994.

- [41] M. A. Mahammed, A. I. Melhum, and F. A. Kochery, "Object distance measurement by stereo vision," *International Journal of Science and Applied Information Technology (IJSAIT)*, vol. 2, no. 2, pp. 05–08, 2013.
- [42] T. E. Oliphant, *A guide to NumPy*. Trelgol Publishing USA, 2006, vol. 1.
- [43] N. Ari and M. Ustazhanov, "Matplotlib in python," in *2014 11th International Conference on Electronics, Computer and Computation (ICECCO)*. IEEE, 2014, pp. 1–6.
- [44] J. L. Guiñón, E. Ortega, J. García-Antón, and V. Pérez-Herranz, "Moving average and savitzki-golay smoothing filters using mathcad," *Papers ICEE*, vol. 2007, 2007.
- [45] C. Vaiphasa, "Consideration of smoothing techniques for hyperspectral remote sensing," *ISPRS journal of photogrammetry and remote sensing*, vol. 60, no. 2, pp. 91–99, 2006.
- [46] M. U. Bromba and H. Ziegler, "Application hints for savitzky-golay digital smoothing filters," *Analytical Chemistry*, vol. 53, no. 11, pp. 1583–1586, 1981.
- [47] R. W. Schafer, "What is a savitzky-golay filter?[lecture notes]," *IEEE Signal processing magazine*, vol. 28, no. 4, pp. 111–117, 2011.
- [48] D. Paret and C. Fenger, *The I2C bus: from theory to practice*. John Wiley & Sons, Inc., 1997.
- [49] C. Liechti, "Pyserial documentation," *Versión: 2.6, Diciembre 2011*, 2016.
- [50] [REDACTED]
- [51] [REDACTED]
- [52] A. R. K. A. Mordvintsev, "OpenCVPython," www.docs.opencv.org/3.0-beta/doc/py_tutorials/py_setup/py_intro/py_intro.html#intro, 2019, online; accessed 29 January 2020.
- [53] J. Deng, J. Guo, Y. Zhou, J. Yu, I. Kotsia, and S. Zafeiriou, "Retinaface: Single-stage dense face localisation in the wild," *arXiv preprint arXiv:1905.00641*, 2019.
- [54] [REDACTED]
- [55] M. K. Alam, N. F. M. Noor, R. Basri, T. F. Yew, and T. H. Wen, "Multiracial facial golden ratio and evaluation of facial appearance," *PloS one*, vol. 10, no. 11, p. e0142914, 2015.

- [85] M. H. Li, A. Yadollahi, and B. Taati, "A non-contact vision-based system for respiratory rate estimation," in *2014 36th Annual International Conference of the IEEE Engineering in Medicine and Biology Society*. IEEE, 2014, pp. 2119–2122.
- [86] S. Ariyaratnam and J. Rood, "Measurement of facial skin temperature," *Journal of dentistry*, vol. 18, no. 5, pp. 250–253, 1990.
- [87] E. Y. Ng, G. Kawb, and W. Chang, "Analysis of ir thermal imager for mass blind fever screening," *Microvascular research*, vol. 68, no. 2, pp. 104–109, 2004.
- [88] R. M. Haralick, H. Joo, C.-N. Lee, X. Zhuang, V. G. Vaidya, and M. B. Kim, "Pose estimation from corresponding point data," *IEEE Transactions on Systems, Man, and Cybernetics*, vol. 19, no. 6, pp. 1426–1446, 1989.
- [89] I. Martinez, "Radiative view factors," *Webserver. dmt. upm. es/~ isidoro/tc3/Radiation% 20View% 20factors. pdf*, 2015.
- [90] S. J. Johnston, P. J. Basford, C. S. Perkins, H. Herry, F. P. Tso, D. Pezaros, R. D. Mullins, E. Yoneki, S. J. Cox, and J. Singer, "Commodity single board computer clusters and their applications," *Future Generation Computer Systems*, vol. 89, pp. 201–212, 2018.
- [91] S. Mittal, "A survey on optimized implementation of deep learning models on the nvidia jetson platform," *Journal of Systems Architecture*, vol. 97, pp. 428–442, 2019.
- [92] A. Eppright and H. Suga, "Hdmi connection system and method for use," Nov. 12 2009, uS Patent App. 12/115,859.